Montclair State University

Montclair State University Digital Commons

Theses, Dissertations and Culminating Projects

5-2023

Parameter Optimization for Excitable Cell Models

Amrit Parmar

Follow this and additional works at: https://digitalcommons.montclair.edu/etd

 Part of the Applied Mathematics Commons, and the Statistics and Probability Commons

Abstract

The electrophysiology of nodose ganglia neurons is of great interest in the analysis of cell membrane currents and action potential behavior. This behavior was initially outlined in the Hodgkin-Huxley conductance model [1] using a system of nonlinear differential equations. Later, Schild et al. [2] developed an extension of the Hodgkin-Huxley model to provide a more exhaustive description of ion channels involved in nodose neuronal action potential activity. We consider a variety of methods to fit the parameters of both the Hodgkin-Huxley and Schild et al. models to an empirical stimulus response dataset. Our methods were validated using synthetic datasets, as well as voltage-clamp data for nodose neurons. The fitting procedure that we implemented demonstrates the predictive efficacy of the Schild et al. model as well as its ability to provide a superior characterization of electrical signatures of nodose neurons.

MONTCLAIR STATE UNIVERSITY

Parameter Optimization for Excitable Cell Models

by

Amrit Parmar

A Master's Thesis Submitted to the Faculty of

Montclair State University

In Partial Fulfillment of the Requirements

For the Degree of

Master of Science

May 2023

College of Science and Mathematics

Department of Applied
Mathematics and Statistics

Thesis Committee:

[redacted]

Dr. Eric Forgoston
Thesis Sponsor

[redacted]

Dr. Elena Petroff
Committee Member

[redacted]

Dr. Baojun Song
Committee Member

PARAMETER OPTIMIZATION FOR EXCITABLE CELL MODELS

A THESIS

Submitted in partial fulfillment of the requirements

For the degree of Master of Science

by

AMRIT PARMAR

Montclair State University

Montclair, NJ

May 2023

Acknowledgements

I want to express my sincerest gratitude to my advisor, Dr. Eric Forgoston, who has been a valued mentor throughout the course of my entire Master's program, encouraging my curiosity as a student, challenging me to be the strongest I've ever been as a thinker and problem solver, and inspiring in me a love for scientific inquiry and research.

I would like to acknowledge the contributions of the late Dr. Vladislav Snitsarev, without whom this work would not have been possible. I am grateful for the time I was able to spend learning from him, and I hope that this work will be a step toward realizing the research vision with which he began this project.

I would like to thank my committee members: Dr. Elena Petroff for supporting the completion of this work with her invaluable insights and experience in neuroscience, and Dr. Baojun Song for sharing his input and expertise in mathematical biology to improve this project.

I want to also thank my family and friends for their unfailing support and encouragement.

Contents

List of Figures

List of Tables

1 Introduction

The ability of excitable cells to generate stimulus responses constitutes a fundamental mechanism of cellular communication in biological organisms. In the human body, several types of cells may be broadly categorized as excitable cells, including neurons, muscle cells, and endocrine cells. Neurons, in particular, transmit electrical and chemical signals throughout the brain and the rest of the body and are responsible for sensory perception, motor control, homeostasis, and adaptation, among other functions. Figure (1a) displays a schematic of a neuron's structure. A cell's excitatory response to a stimulus, such as synaptic activity or receptor activation, is known as an action potential. This phenomenon is characterized by a rapid change in voltage across the cell membrane, which in neurons occurs when they undergo a shift in membrane potential due to the movement of ions through membrane channels. Figure (1b) displays a schematic of the neuron's semi-permeable membrane. The resting membrane potential in neurons typically falls near -70 mV. It is dependent on the types of open ion channels and the concentrations of different ions present in the intracellular and extracellular fluids during the resting state [8].

1.1 The Action Potential

The stimulus which initiates an action potential in a neuron causes its membrane potential to gradually become less negative. If the membrane potential reaches a threshold value, typically around -55 mV, an action potential will be generated. Once the threshold value is reached, the cell undergoes the depolarization phase of the action potential, where voltage-gated sodium channels are opened, and Na^+ ions flow into the cell. This reverses the resting polarity of the cell, and the interior of the cell now becomes more positive than the exterior of the cell. If the threshold value is not reached, an action potential will not be generated. An inadequate current injection will not result in a partial action potential, nor will an excessive current injection result in a greater depolarization potential inside the cell. This is known as the "all-or-nothing" characteristic of the action potential [9].

As the cell depolarizes, the voltage-gated sodium channels inactivate, and the highly positive potential inside the cell causes the voltage-gated potassium channels to open. Once the maximum potential is reached, voltage-gated potassium channels are fully activated, allowing K^+ ions to flow out of the cell en masse in a process known as repolarization. In this phase of the action potential, the cell restores its negative potential by releasing the positively charged potassium ions. Repolarization typically undershoots the resting membrane potential, resulting in what is known as the hyperpolarization phase, where the interior potential of the cell becomes more negative than its resting potential. This is followed by a refractory period, during which the cell restores its initial concentrations of Na^+ and K^+ ions inside and outside the cell and reestablishes the resting membrane potential [8]. The entire action potential process, which occurs within the span of 1-5 milliseconds, causes an electric impulse to be carried down an axon of a neuron via the flow of ions in and out of the cell. Upon reaching the axon terminal, an action potential signal typically

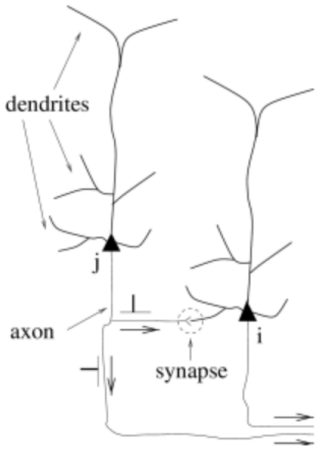

(a) Schematic of a neuron's anatomical structure: dendrites, axons, and the synaptic gap [3].

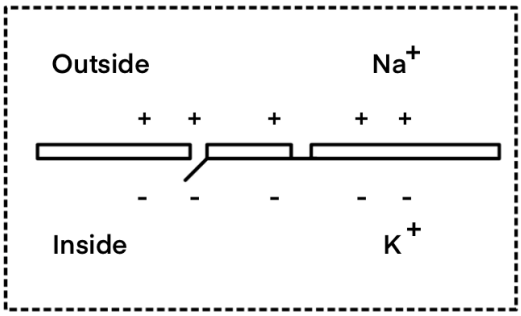

(b) Schematic of the semi-permeable cellular membrane of a neuron, through which the flow of Na^+ and K^+ ions facilitates changes in the potential difference between the inside and outside of the membrane. Image based on figure from Ref. [3].

Figure 1: Action potentials, generated by the movement of Na^+ and K^+ ions through the cellular membrane, propagate down axons until they reach a synaptic gap, where they elicit the release of neurotransmitters or chemical messengers to communicate with other cells [3].

causes the release of neurotransmitters at the synapse — the junction between two neurons. Neurotransmitters are molecules that support a wide array of functions and can activate or inhibit the action of neurons or other postsynaptic cells [10].

The action potential is understood to be the fundamental constituent of nervous system activity, responsible for detecting external stimuli, integration of sensory input, motor control, and cognition, among other functions. Action potential activity is further known to facilitate synaptic plasticity, where the strength of a synapse is modified in response to its own activity or through activity in another pathway. The action potential, therefore, is an essential element in not only the mechanisms by which an organism's nervous system may process information and communicate with other organ systems but also the mechanisms by which it may adapt and grow. It is the process through which rapid communication occurs between neurons over long distances and allows organisms to function as they do [11]. Given that action potentials are responsible for so many crucial biological mechanisms, a thorough understanding of their behavior is necessary for understanding communication, sensory processing, plasticity, and regulation within organisms.

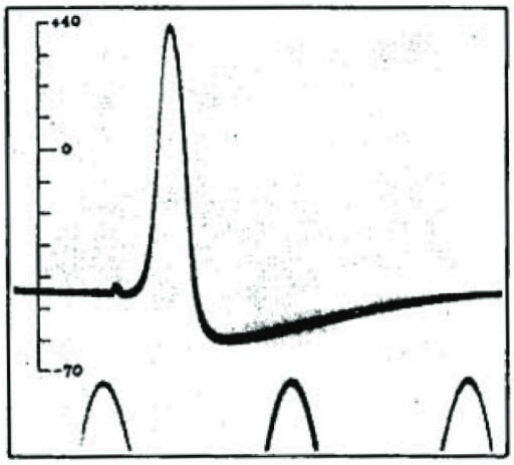

Figure 2: The action potential measured in millivolts inside the giant axon of the long-finned squid by Hodgkin and Huxley [4].

2 Neurophysiological Modeling

Neurophysiological modeling aims to employ mathematical representations to characterize the behavior of nerve cells. These models can provide numerical descriptions of nerve cells and investigate the mechanisms of their stimulus responses observed in experimental data. Superior modeling of the electrophysiology of neurons can be used to better understand abnormal behavior of neurons, such as behavior under the effects of neurotoxins, in the presence of pharmaceuticals that target ion channels and their mechanisms of action, or in the presence of neurological disorders like epilepsy and Parkinson's disease. It may also be used to better demonstrate the regulatory roles neurons play in homeostatic mechanisms, such as the baroreceptor reflex [2].

2.1 The Hodgkin-Huxley Model

The Hodgkin-Huxley (HH) conductance model laid the groundwork for modern neurophysiological modeling. Published in 1952 by Alan Hodgkin and Andrew Huxley, this model was based on the giant axon of a long-finned squid (*Loligo forbesii*), which was approximately 500 micrometers in diameter [1]. Figure (2) shows one of the action potentials recorded by Hodgkin and Huxley from the squid's axon [4]. The HH model, based on replicating the activity displayed in such recordings, describes the underlying mechanisms of experimentally observed ion dynamics and the generation of voltage spikes in the squid's axon. This model encapsulated these dynamics within a system of nonlinear differential equations. Differential equations describe the relationship between functions, in this case representing physical quantities, and their rates of change. Solving the HH equations returns a simulation of the behavior of neuron action potentials. These equations include parameters that may be adjusted or fine-tuned to mimic different states of the neuron.

This model demonstrated that the action potential could be characterized in terms of ionic currents, namely: the Na^+, K^+, and leak currents. Representing the axon

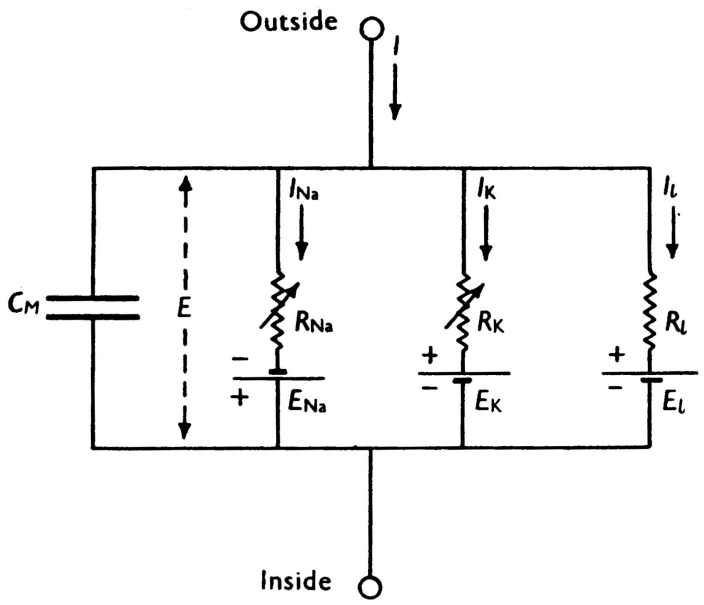

Figure 3: Electrical equivalent circuit for a short segment of squid giant axon. Here, C_m is the membrane capacitance representing the lipid bilayer, R_{Na} and R_K are resistors representing the voltage-gated ion channels, R_L is the resistor representing leak ion channels, E_{Na}, E_K, and E_L are battery representations of the electrochemical gradients driving voltage-gated ion flow and leak ion flow, respectively, and I_{Na}, I_K, and I_L represent ion pumps and exchangers as current sources [5].

as an equivalent parallel circuit, as shown in Fig. (3), the HH model allowed for the generation of action potential signatures using capacitors, resistors, and batteries - translating a biological system into an analogous physical system operating under the laws of pre-existing electromagnetic theory.

The semi-permeable neuronal membrane is represented by a capacitor, C_m, as it separates ionic charge on either side of the membrane. In addition to helping specific ions permeate through the membrane, the current flow charges the membrane capacitance. As ions actively permeate through the membrane, the intracellular concentrations of those ions differ from their extracellular concentrations. This difference in ion concentration produces a potential difference between the inside and outside of the membrane, which further determines the tendency of ions to flow back and forth through the membrane. The potential at which the direction of current flow reverses is known as the Nernst reversal potential, represented as a battery for each ion [5].

As batteries, the three Nernst potentials, E_{Na}, E_K, and E_L, drive ion flow within the circuit. The voltage-gated sodium, voltage-gated potassium, and leak ion channels are represented by resistors, R_{Na}, R_K, and R_L, respectively, as they control the flow of ions between the inside and outside of the cell. Each channel's resistor may be described by its conductance, the reciprocal of its resistance. The sodium and potassium channels are voltage-dependent; they open or close depending on the membrane potential, and therefore, their conductances are functions of voltage and time. The

leak ion channel, which accounts for other ions like chloride, is considered to remain open throughout the entire duration of an action potential; thus, its conductance is neither voltage- nor time-dependent. While the Na^+ and K^+ ion channels are responsible for generating the action potential, the leak channels, which have relatively low conductance, are responsible for maintaining the resting membrane potential [3, 5].

The foremost equation, which characterizes the behavior of the electrical equivalent circuit shown in Fig. (3), is given by

$$C_m \frac{dV}{dt} + I_{ion} = I_{ext}. \tag{1}$$

Equation (1) expresses the relationship between the rate of change of the membrane potential and the ions permeating through the cell membrane. The term I_{ion} is itself the sum of ionic currents, and each current has the form

$$I_{ion} = \sum_j I_j = \sum_j g_j(V - E_j), \tag{2}$$

where g_j is the conductance of the j-th current, V is the membrane potential, and E_j is the Nernst potential for the j-th current. If the membrane potential is equal to the Nernst potential for any of the ion channels, the difference between the two will equal zero, and no current of that ion will flow. Equation (2) may be expanded to include the inward sodium current, I_{Na}, outward potassium current, I_{K}, and leak current, I_L, so that it becomes

$$I_{ion} = g_{\mathrm{Na}}(V - E_{\mathrm{Na}}) + g_{\mathrm{K}}(V - E_{\mathrm{K}}) + g_L(V - E_L). \tag{3}$$

In this model, the sodium and potassium currents are taken to be voltage-dependent, while the leak current is considered constant. The ion channels consist of gates that must all be open at once in order for an ion to pass through; if all of the gates are open, such a channel is said to be in a permissive state. If even one of the gates is closed, an ion cannot flow through, and the channel is said to be in a non-permissive state [5]. The state of a gate, either permissive or non-permissive, is a voltage-dependent characteristic. Therefore, the probability of a gate being open, also known as a gating variable, is a function of voltage and time. These gates are assumed to operate independently of each other. Therefore, the total probability of a channel being open is given simply by the product of the individual gate probabilities, p_r. The overall conductance of a channel is given by

$$g_j = \bar{g}_j \prod_r p_r, \tag{4}$$

where $\bar{g}_j$ is the maximum conductance of the j-th current.

As per the form displayed in Eqn. (4), sodium and potassium conductances are functions of their respective maximum conductances, $\bar{g}_{Na}$ and $\bar{g}_K$, the conductance value when the channel is in a permissive state, and the gating variables. There are two types of gates considered in the ion channels: activation gates and inactivation

gates. The probability of an activation gate being open increases as depolarization progresses, whereas the probability of an inactivation gate being open decreases as depolarization progresses. The voltage-gated sodium channel possesses three rapidly acting activation gates, or m-gates, and a single slow-acting inactivation gate, or h-gate. Therefore, overall conductance of sodium is given by

$$g_{\mathrm{Na}} = \bar{g}_{\mathrm{Na}} m^3 h. \tag{5}$$

While the cell membrane is at resting potential, the sodium h-gate is open, and the m-gates are closed. As depolarization occurs, the m-gates rapidly open, and the entire channel is in a permissive state, allowing Na^+ ions to flood into the cell. The h-gates close shortly thereafter, inactivating the channel and preventing any more influx of Na^+ ions. In a typical action potential process, the cell membrane then repolarizes, causing the m-gates to rapidly close as well. Even if the membrane were to be depolarized from this state and the m-gates re-opened, the slow-acting h-gate would remain closed, thereby keeping the entire channel in a non-permissive state. If, however, the membrane were to be held in a repolarization phase after the initial depolarization, the h-gates would eventually re-open, restoring the resting state of the voltage-gated sodium channel: an open h-gate and closed m-gates [5].

A potassium channel possesses four activation gates, all of which must be open for a potassium ion to pass through the gate. Therefore, the potassium conductance is given by

$$g_{\mathrm{K}} = \bar{g}_{\mathrm{K}} n^4. \tag{6}$$

During depolarization, the slow-acting n-gates open gradually, shifting the voltage-gated potassium channel to a permissive state. This channel remains in a permissive state for the entirety of the depolarization phase, but its n-gates begin to slowly close during the repolarization phase, allowing a sufficient number of K^+ ions to be expelled from the cell [5]. As the leak channel is considered to be always open in this model, its conductance, g_L, is simply its maximum conductance, $\bar{g}_L$. This relation is expressed by

$$g_L = \bar{g}_L, \tag{7}$$

where the leak channel is always operating at its maximum conductance. Given this information, Eqn. (3) becomes

$$I_{ion} = \bar{g}_{\mathrm{Na}} m^3 h(V - E_{\mathrm{Na}}) + \bar{g}_{\mathrm{K}} n^4 (V - E_{\mathrm{K}}) + \bar{g}_L (V - E_L). \tag{8}$$

Table 1 displays Hodgkin and Huxley's empirically determined values of the parameters in this equation. Substituting Eqn. (8) into the equation describing the net electrical circuit behavior, Eqn. (1), and isolating the time rate of change of membrane potential, $\frac{dV}{dt}$, yields

$$\frac{dV}{dt} = \frac{1}{C_m}[I_{ext} - [\bar{g}_{\mathrm{Na}} m^3 h(V - E_{\mathrm{Na}}) + \bar{g}_{\mathrm{K}} n^4 (V - E_{\mathrm{K}}) + \bar{g}_L (V - E_L)]]. \tag{9}$$

The gating variables, m, h, and n, are themselves functions of both voltage and time, and their time rates of change are defined in Eqns. (10)-(12). The α_r and β_r rate

Constants	Description
$C_m = 1.0\frac{\mu F}{cm^2}$	Membrane capacitance
$\bar{g}_{\text{Na}} = 120\frac{mS}{cm^2}$	Sodium maximum conductance
$\bar{g}_{\text{K}} = 36\frac{ms}{cm^2}$	Potassium maximum conductance
$\bar{g}_L = 0.3\frac{ms}{cm^2}$	Leak maximum conductance
$E_{\text{Na}} = 50.0mV$	Sodium reversal potential
$E_{\text{K}} = -77.0mV$	Potassium reversal potential
$E_L = -54.387mV$	Leak reversal potential

Table 1: Parameter values of the standard HH model, as determined experimentally by Hodgkin and Huxley [5].

constants represent the rate at which closed channels open and the rate at which open channels close, respectively, for the sodium activation, sodium inactivation, and potassium activation channels.

The time rate of change of a gating variable is determined by the rate at which these channels change from open to closed and from closed to open at any given time [5] and is given by

$$\frac{dm}{dt} = \alpha_m(V)(1-m) - \beta_m(V)m, \tag{10}$$

$$\frac{dh}{dt} = \alpha_h(V)(1-h) - \beta_h(V)h, \tag{11}$$

$$\frac{dn}{dt} = \alpha_n(V)(1-n) - \beta_n(V)n. \tag{12}$$

Taken together, Eqns. (9)-(12) constitute the governing equations of the HH model. The initial conditions needed to solve these equations may be obtained from the rest state values of the gating variables when V=0 mV. These values are given by

$$m_0 = \frac{\alpha_{m_0}}{\alpha_{m_0} + \beta_{m_0}}, \tag{13}$$

$$h_0 = \frac{\alpha_{h_0}}{\alpha_{h_0} + \beta_{h_0}}, \tag{14}$$

$$n_0 = \frac{\alpha_{n_0}}{\alpha_{n_0} + \beta_{n_0}}. \tag{15}$$

Using the above conditions, $m = m_0$, $h = h_0$, and $n = n_0$ when $t = 0$, we arrive at the following solutions of Eqns. (10)-(12) defining the gating variables as

$$m = m_\infty - (m_\infty - m_0)\exp(-t/\tau_m), \tag{16}$$

$$h = h_\infty - (h_\infty - h_0)\exp(-t/\tau_h), \tag{17}$$

$$n = n_\infty - (n_\infty - n_0)\exp(-t/\tau_n), \tag{18}$$

where m_∞, h_∞, and n_∞ are the steady-state values of the gating variables of sodium activation, sodium inactivation, and potassium activation, respectively. The associated time constants for each gating variable are given by τ_m, τ_h, and τ_n [5]. These values are defined as

$$m_\infty = \alpha_m/(\alpha_m + \beta_m), \tag{19}$$
$$\tau_m = 1/(\alpha_m + \beta_m), \tag{20}$$
$$h_\infty = \alpha_h/(\alpha_h + \beta_h), \tag{21}$$
$$\tau_h = 1/(\alpha_h + \beta_h), \tag{22}$$
$$n_\infty = \alpha_n/(\alpha_n + \beta_n), \tag{23}$$
$$\tau_n = 1/(\alpha_n + \beta_n). \tag{24}$$

Finally, the voltage-dependent rate parameters α_r and β_r of the ion channel gates are considered [5]. The parameters for the m and h-gates of the sodium channel are given by

$$\alpha_m = \frac{0.1(V+25)}{e^{\frac{V+25}{10}} - 1}, \tag{25}$$
$$\beta_m = 4e^{\frac{V}{18}}, \tag{26}$$
$$\alpha_h = 0.07e^{\frac{V}{20}}, \tag{27}$$
$$\beta_h = \frac{1}{e^{\frac{V+30}{0.10}} + 1}. \tag{28}$$

The parameters of the n-gate are similarly given by

$$\alpha_n = -\frac{0.01(V+10)}{e^{\frac{V+10}{10}} - 1}, \tag{29}$$
$$\beta_n = 0.125e^{\frac{V}{80}}. \tag{30}$$

This groundbreaking work won its authors the Nobel Prize in Medicine and Physiology in 1963. Although it took decades to computationally confirm the predictions made by the model, it has served as a foundation for a vast number of contemporary neuronal models. The HH model is widely considered to have marked the beginning of the field of computational neuroscience. However, given the amount of specialization which cells undergo during an organism's developmental stages, the HH model alone could not have captured the behavior of the diverse range of neuron types that have been identified in the decades since its creation. Instead, the HH model has served as a template for modeling other types of neurons and expanding the number of considered variables in order to account for more sophisticated cellular dynamics.

2.2 The Nodose Neuron

One such specialized cell type is the vagal afferent neuron of the nodose ganglion. These neurons are located in the nodose ganglion, also known as the inferior ganglion, of the vagus nerve. This ganglion is part of the peripheral nervous system, which is composed of nerves and ganglia outside the brain and spinal cord. Figure (4) shows an anatomical schematic of the vagus nerve system where the nodose ganglion is located. Baroreceptor sensory neurons are a sub-type of vagal afferent nodose neurons. The excitations of baroreceptor neurons are produced by stretches in blood vessels due to increases in blood pressure. These neurons respond to changes in blood pressure by sending signals to the central nervous system, which then activates reflexes that regulate blood pressure via the efferent system [12, 13].

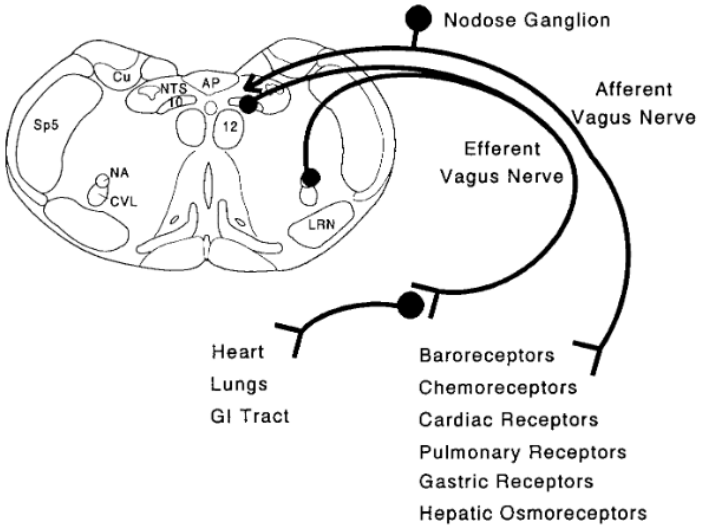

Figure 4: Schematic diagram of the anatomy of the afferent and efferent systems of the vagus nerve [6].

For example, when blood pressure increases, baroreceptor neurons signal to the brain to activate the parasympathetic nervous system, which slows down an organism's heart rate in an effort to lower blood pressure. Conversely, low blood pressure results in a lack of activation of the baroreceptor neurons, which disinhibits the heart's pumping, allowing heart rate and blood pressure to increase until normal levels are reached. This regulation system, which helps to cause an organism's blood pressure to generally exist within a narrow range, is known as the baroreceptor reflex. The baroreceptor reflex is a crucial homeostatic mechanism that ensures adequate blood flow to vital organs and tissues while maintaining safe levels of cardiac activity [12,13].

In a seminal work by Schild et al. [2] to characterize the mechanisms of the baroreceptor reflex, two populations of rat nodose sensory neurons, categorized as A-type and C-type, were examined. A-type nodose neurons, which are less frequently observed within an organism's nervous system, possess myelinated axons. These axons are sheathed in a mostly lipid membrane known as myelin, which increases the conduction velocity of the electrical signal transmitted along them [13]. C-type nodose

neurons are unmyelinated. The action potentials of A-type cells are of a shorter duration than action potentials in C-type cells. Signal transmission occurs with a much lower conduction velocity in C-type cells than in A-type cells. A-type action potentials also lack a definite inflection during the repolarization phase and possess a shorter duration after-hyperpolarization phase than C-type nodose neurons [2]. In this work, we consider A-type rat nodose neurons.

2.3 The Schild et al. Extended Model

The study described in Sec. 2.2 resulted in the Schild et al. conductance (SC) model of rat nodose neurons [2]. This model, which may be considered an extension of the HH model, consists of 19 differential equations formulated for all of the ionic membrane currents considered for the nodose neuron. Just as in the HH model, an equivalent parallel conductance model was constructed to analyze the cell's electrophysiology in terms of physical units - capacitors, resistors, and batteries. Compared to the HH model, however, this model's significantly more complex differential equation system yields more sophisticated modeling capabilities.

This model, represented in Fig. (5), consists of two main components: a membrane model and a coupled fluid compartment model. The membrane model considers membrane potential, which measures the difference in electric potential between the interior and exterior of the cell. This component of the model describes the changes in voltage across the neuronal membrane over time. The fluid compartment model accounts for the dynamics of Ca^{2+} ions by considering three separate fluid compartments: the intracellular medium Vol_i, the perineuronal medium Vol_s, and the surrounding extracellular volume. The Ca^{2+} ion exchanges are considered locally between the intracellular and perineuronal compartments in the presence of a calmodulin-type buffer, whereas ionic concentrations in the extracellular compartment $[Ca^{2+}]_o$,$[Na^+]_o$, and $[K^+]_o$ are considered constant [2].

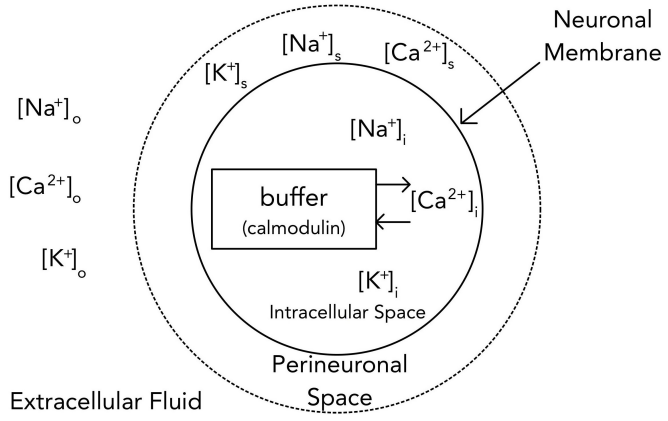

Figure 5: Fluid compartment model consisting of 3 separate compartments with differing concentrations of Na^+ K^+, and Ca^{2+}: intracellular space, perineuronal annular space, and a large extracellular volume. Image based on figure from Ref. [2].

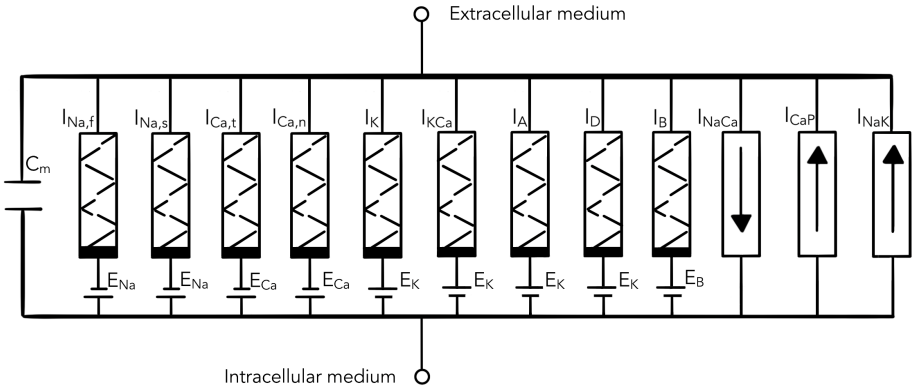

Figure 6: Equivalent parallel conductance circuit of the rat nodose neuron involving time and voltage-dependent Na^+ K^+, and Ca^{2+} channel-mediated currents; the circuit corresponds to a 19-component system of differential equations. Image based on figure from Ref. [2].

The SC model is formulated starting with a generalized description of whole-cell currents in the form of the HH equations, given by

$$I_j(t,V) = \bar{g}_j m_j^x(t,V) h_j^y(t,V)(V - E_j). \tag{31}$$

Here, just as in the HH model, $\bar{g}_j$ is the maximum conductance of an ion j, m_j represents the activation gating variable of j and is raised to an integer exponent, x, which denotes the number of activation gates per channel. Similarly, h represents the inactivation gating variable of ion j and is raised to an integer exponent, y, which denotes the number of inactivation gates per channel. The term V is the membrane potential, and E_j is the Nernst reversal potential for the relevant ion j. [2].

It is worth noting that while in the HH model, I was considered in $\mu A/cm^2$, the SC model considers I in nA. This conversion is based on an assumption behind the SC model, where the soma of a nodose neuron is considered as a sphere of radius 15 μm with a total membrane capacitance of approximately 40 pF. This corresponds to a specific capacitance of 1.4 $\mu F/cm^2$, quite similar to the HH specific capacitance of 1.0 $\mu F/cm^2$. For the A-type neuron, the membrane capacitance is specified to be 32.5 pF [2].

Gating variables, z, are defined implicitly via their time rates of change in differential equations of the form

$$\dot{z} = \frac{(z_\infty - z)}{\tau_z}. \tag{32}$$

Here z_∞ is the steady-state value of the gating variable, and τ_z is the associated time constant. z_∞ is described in a standard manner for all currents involved in the circuit by

$$z_\infty(V) = \frac{1.0}{1.0 + \exp\left(\frac{V_{1/2} - V}{S_{1/2}}\right)}. \tag{33}$$

The term $V_{1/2}$ is defined as the half-activation potential, and $S_{1/2}$ is a value related to the reciprocal of the slope of the activation curve measured at $V_{1/2}$ [2]. A single

Gaussian form is used to define τ_z for both activation and inactivation gates, given by

$$\tau_z = A \exp\left(-B^2(V - V_{peak})^2\right) + C. \tag{34}$$

Here A corresponds to the peak amplitude of the time constant function, B is a width scaling factor, V_{peak} is the membrane potential at which τ_z equals A, and C is a shifting parameter.

Equations can be further formulated for each ionic membrane current in the model, which consists of lumped membrane capacitance, C_m, associated with various ion channels and currents. To model the electrical properties of the neuron, the equivalent membrane circuit in Fig. (6) is considered. It consists of the membrane capacitance, C_m, shunted by time- and voltage-dependent sodium, calcium, and potassium currents I_{Na_f}, I_{Na_s}, I_{Ca_t}, I_{Ca_n}, and I_{K}, respectively. Calcium-activated potassium current, $I_{\mathrm{K,Ca}}$, transient outward current, I_A, delay current, I_D, and linear leakage current, I_B, are also involved. Finally transporter-mediated currents, the $\mathrm{Na}^+ - \mathrm{Ca}^{2+}$ exchanger, the $\mathrm{Na}^+ - \mathrm{K}^+$ pump, and the Ca^{2+} pump, are considered. The equilibrium potentials for the sodium, potassium, calcium, and background ionic channels are denoted by E_{Na}, E_{K}, E_{Ca}, and E_B, respectively [2]. The differential equation expressing the time rate of change of membrane potential, V, may be derived from the circuit in Fig. (6), and is given by

$$\dot{V} = -\frac{\Sigma I_{ion} - I_{ext}}{C_m}. \tag{35}$$

Here I_{ion} corresponds to individual currents shown in the circuit in Fig. (6), and I_{ext} corresponds to either the voltage-clamp evoked current or the current-clamp injected current. Differential equations for $z = m_f$, h_f, h_s, d_t, f_t, d_n, f_{n1}, f_{n2}, n, p, q, x, y, and c can be formulated in the form of HH-type differential equations using Eqns. (31)-(34). Tables 15-18 of the Appendix describe the full set of equations and their associated parameters. Table 17 of the Appendix provides the model equations for the four outward potassium currents [2].

An HH-type model is not complete without a consideration of ion exchange mechanisms and ATP-dependent pumps, which maintain intracellular homeostasis. The sodium-calcium exchanger $I_{\mathrm{Na,Ca}}$, electrogenic calcium pump $I_{\mathrm{Ca}P}$, and electrogenic activated potassium pump $I_{\mathrm{K,Ca}}$ are responsible for the active transport of Na^+, Ca^{2+}, and K^+ across the semi-permeable membrane [2]. These currents and their equations are detailed in Table 18 of the Appendix.

The governing equations of the fluid compartment are given in Eqns. (36) - (38). The derivation of these equations can be found in Ref. [2]. The rate of change with respect to time of occupancy of a non-organelle-related intracellular buffer is given by

$$\dot{O}_c = k_U[\mathrm{Ca}^{2+}]_i(1 - O_c) - k_R O_c. \tag{36}$$

Here O_c is the buffer occupancy, k_U is the kinetic rate constant for Ca^{2+} uptake, and k_R is kinetic rate constant for Ca^{2+} release [2]. The rate of change of intracellular

Ca^{2+} ion concentration is described by

$$[\dot{Ca^{2+}}]_i = \frac{2I_{\mathrm{Na,Ca}} - I_{\mathrm{Ca},n} - I_{\mathrm{Ca},t} - I_{B,\mathrm{Ca}} - I_{\mathrm{Ca}P}}{Z_{\mathrm{Ca}} Vol_i F} - n_b [B]_i \dot{O}_c. \tag{37}$$

Here Z_{Ca} is the valence, F is Faraday's constant, and Vol_i is the effective cell volume [2]. The Ca^{2+} balance within the external perineuronal space (Vol_s), is given by

$$[\dot{Ca^{2+}}]_s = \frac{[Ca^{2+}]_o - [Ca^{2+}]_s}{\tau_{\mathrm{Ca}}} + \frac{-2I_{\mathrm{Na,Ca}} + I_{\mathrm{Ca},n} + I_{\mathrm{Ca},t} + I_{B,\mathrm{Ca}} + I_{\mathrm{Ca}P}}{Z_{\mathrm{Ca}} Vol_s F}, \tag{38}$$

where τ_{Ca} is the time constant for the relatively slow Ca^{2+} diffusion between the perineuronal volume and the bathing medium, and Vol_s is the annular shell thickness of the perineuronal space [2]. The parameter values needed for the full A-type model, including the fluid compartment model, are displayed in Table 2.

3 Methods

In this project, we developed a methodology for evaluating the HH model and its extension, the SC model, with respect to their ability to characterize experimentally recorded stimulus response data from rat nodose neurons. This required constructing a program to solve the HH and SC equations using numerical methods and then optimizing the parameters of both models, shown in Tables 1 and 2, such that their solutions would produce minimal error with respect to the data.

3.1 Data Collection and Analysis

In this study, action potential data collected from Sprague-Dawley rats was used to investigate the properties of nodose ganglia cells. The rat neurons were cultured by dissecting the nodose ganglia, preparing its slices with digestive enzymes, and bathing them in biochemical suspensions. These cell specimens were divided into groups, where some were used to produce voltage-clamp recordings and the rest for current-clamp recordings. The process by which the neurons were isolated and cultured is described in further depth in Ref. [14]. The voltage-clamp technique allows one to hold the membrane potential constant at a predetermined value and measure the current flow. The current-clamp technique similarly allows one to hold the transmembrane current at a known value and measure the transmembrane voltage response [15].

We consider current-clamp recording data in this work. The current-clamp technique typically involves an intracellular microelectrode containing a conductive solution and an extracellular reference electrode to record the potential difference across the cell membrane. At the same time, a current is injected into the cell. This allows for the measurement of transmembrane voltage in isolated tissue preparations such as the nodose neuron preparation described above [14, 15].

Figure (7) displays the current-clamp stimulus response and current injection time series data that we consider in this work, recorded over 819.2 ms. The current injections made were 0 nA from approximately 0 to 100 ms, -0.1 nA from approximately

Model Parameters	Conductances for A-type neuron model
$[\mathrm{Na}^+]_i = 8.9mM$	$\bar{g}_{\mathrm{Na}_f} = 2.0500\mu S$
$[\mathrm{Na}^+]_o = 154.0nM$	$\bar{g}_{\mathrm{Na}_s} = 0.00001\mu S$
$[\mathrm{K}^+]_i = 145.0mM$	$\bar{g}_{\mathrm{Ca}_t} = 0.00035\mu S$
$[\mathrm{K}^+]_o = 5.4mM$	$\bar{g}_{\mathrm{Ca}_n} = 0.00100\mu S$
$[\mathrm{Ca}^{2+}]_o = 2.0mM$	$\bar{g}_{\mathrm{K}} = 0.00550\mu S$
$\tau_{\mathrm{Ca}} = 4511.0ms$	$\bar{g}_A = 0.03500\mu S$
$E_{\mathrm{Na}} = 72.7194mV$	$\bar{g}_D = 0.0100\mu S$
$E_{\mathrm{K}} = -83.9282mV$	$\bar{g}_{\mathrm{K,Ca}} = 0.00650\mu S$
$[B]_i = 0.001mM$	$\bar{g}_{B,\mathrm{Ca}} = 0.000085\mu S$
$R = 8.314Jmole^{-1}K^{-1}$	$\bar{g}_{B,\mathrm{Na}} = 0.000325\mu S$
$F = 96500Cmole^{-1}$	$\bar{I}_{\mathrm{Ca}P} = 0.0243nA$
$T = 296K$	$\bar{I}_{\mathrm{NaK}} = 0.275nA$
$K_{M,\mathrm{Na}} = 5.46mM$	$C_m = 32.5pF$
$K_{Na,\mathrm{Ca}} = 0.000036nAmM^{-4}$	
$K_{M,\mathrm{K}} = 0.621mM$	
$k_U = 100mM^{-1}mS^{-1}$	
$k_R = 0.238ms^{-1}$	
$Z_{\mathrm{Ca}} = 2.0$	
$\gamma = 0.5$	
$r = 3$	
$n_b = 4$	
$Vol_i = 0.0127nl$	
$Vol_s = 0.0146nl$	

Table 2: The model parameters and ion channel conductances for the A-type nodose neuron, as determined experimentally by Schild et al. [2].

100 to 350 ms, 0 nA from approximately 350 to 550 ms, 0.1 nA from approximately 550 to 800 ms, and 0 nA from approximately 800 to 819.2 ms. As can be seen in Fig. (7), the recorded measurements of both the injected current and stimulus response are noisy.

3.2 Numerical Integration Methods

As mentioned earlier, differential equations contain information about the relationship between a function and its derivatives, which are themselves functions describing the rates of change of the original function. These equations can serve as descriptions of rapidly changing physical values, such as voltage, which may be too complex to

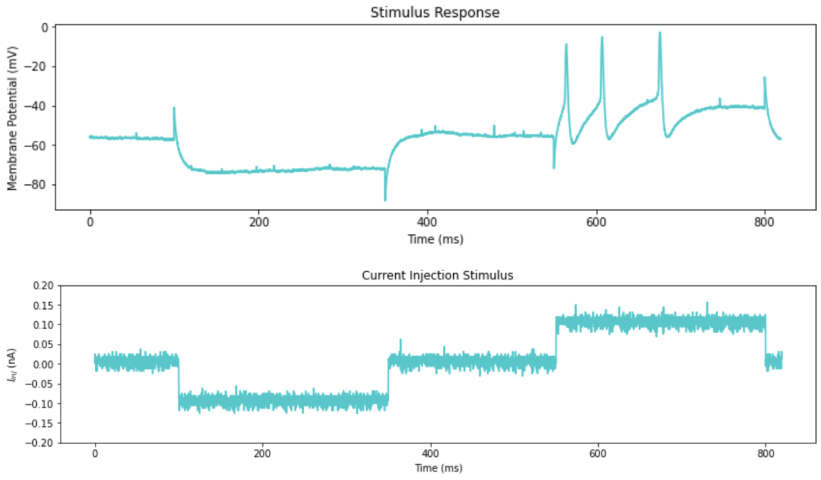

Figure 7: (*Top*) Nodose neuron current-clamp stimulus response time series, where membrane potential is measured in mV and time in ms. *(Bottom)* Associated current injection time series, where current is measured in nA and time in ms.

describe directly. For example, both the HH and SC models contain differential equations involving the rate of change of voltage with respect to time rather than a function of voltage defined in terms of time directly, as displayed in Eqns. (1) and (35).

Some differential equation systems may be analytically solvable and may yield explicit solutions in the form of equations. However, differential equation systems describing real-world phenomena are often analytically intractable; therefore, computational algorithms, such as Runge-Kutta methods or adaptive step-size methods, must be implemented to approximate their solutions numerically. In general, these methods compute solutions by discretizing the differential functions and applying iterative techniques with either fixed or adaptive step-sizes over the interval of interest to form a continuous approximation of the solution [16]. There exists a wide variety of numerical methods which can be used to approximate the solution of differential equations. In this work, to solve the HH and SC systems, we employed the adaptive step-size solver odeint, contained within the SciPy library of the Python programming language. All of the computations were performed in Python 3.9, running on a machine with an AMD Ryzen 9 5900X 12-core processor and an NVIDIA RTX 3080 graphics card.

3.3 Error Minimization Methods

Reliably solving the HH and SC equations was the first step in being able to fit the solutions of the SC model to the experimental nodose neuron data. In the next step, we used an error minimization routine to compute the difference between the time series solution provided by the numerical solver and the time series of the data

itself and to iteratively reduce this difference as much as possible by modifying the parameters of the ordinary differential equation (ODE) model. The error between the numerical solution to the ODE system and empirical data can be represented by a function known as the cost function. Successfully minimizing the cost function was a crucial second step in establishing that the SC model sufficiently characterized the underlying dynamics at work in the nodose neuron.

We could have attempted to optimize the cost function using any of the various minimization techniques included in Python's lmfit.minimize module. While both local and global optimization techniques were available for use, global optimization techniques are generally considered to be superior optimization methods as they seek the combination of parameters that return the minimum error value in the entire search domain. They do, however, tend to carry significantly more computational overhead than local optimization techniques.

We first evaluated the global optimization techniques within the lmfit.minimize module for their efficacy in fitting the following seven parameters of the classic HH model with respect to data generated with the SC model: C_m, $\bar{g}_{\mathrm{Na}}$, $\bar{g}_{\mathrm{K}}$, $\bar{g}_L$, E_{Na}, E_{K}, and E_L. After that, we applied the same fitting techniques to optimize the following ten parameters of the SC model with respect to data generated with the SC model: $\bar{g}_{\mathrm{Na}_f}$, $\bar{g}_{\mathrm{Na}_s}$, $\bar{g}_{\mathrm{K}}$, $\bar{g}_{B,\mathrm{Na}}$, $\bar{g}_A$, $\bar{g}_D$, $\bar{g}_{\mathrm{K,Ca}}$, $\bar{g}_{B,\mathrm{Ca}}$, $\bar{g}_{\mathrm{Ca}_t}$, and $\bar{g}_{\mathrm{Ca}_n}$. The two global optimization techniques we employed are known as Adaptive Memory Programming for Global Optimization (AMPGO) and Differential Evolution (DE). We targeted the fitting code to be run on the NVIDIA graphics card using Python's numba.jit module, which significantly reduced computational times.

3.3.1 AMPGO

AMPGO is an algorithm that operates by using a tunneling method, known as the tabu tunneling method (TTM), to avoid the values being optimized getting stuck in the local minima of the cost function. This is an extension of the well-known pure tunneling method, which alternates between minimization and tunneling phases until a cutoff value is reached. Minimization applies a descent algorithm to find a local minimum. Tunneling then seeks a point with an error less than or equal to that local minimum. The pure tunneling method, however, may fail to find any point which satisfies this criterion in a single iteration. The AMPGO algorithm is designed to overcome this limitation via its TTM, where it implements a short-term memory strategy to perform multiple iterations for a point with an error less than or equal to a given local minimum [17].

3.3.2 DE

DE is a stochastic, population-based algorithm that considers populations of parameter vectors. Evolutionary algorithms like DE follow the general form of cycling through the stages of initialization, mutation, recombination, and selection. Initialization involves the random selection of parameter vectors. Mutation expands the search space by randomly selecting three new vectors for each of the initial parameter

vectors and calculates a single donor vector using all three of these vectors for each initial vector. Recombination uses elements from the initial vector and donor vector to develop a new vector, called a trial vector. Finally, the selection phase compares the error associated with the trial vector to the error associated with the initial vector and selects the one with the lower error to move on to the next generation. Mutation, recombination, and selection are repeated until a threshold tolerance value, or stopping criterion is reached. This method has been found to be more efficient in certain applications than other global optimization techniques, like simulated annealing, evolutionary programming, and genetic algorithms [18, 19].

4 Results

4.1 Fitting the Models to Synthetic Data

The first fitting evaluation involved using synthetically generated data of a single action potential from the HH model. Using the HH model, we produced a time series of 5000 data points spanning 500 ms using the literature parameter values shown in Table 1 and a current injection of $I_{ext} = 3.0\mu A/cm^2$ applied from 100 to 200 ms. We then treated this time series like empirical stimulus response current-clamp data, where the parameters were unknown. Both the AMPGO and DE methods were then applied in an attempt to recover the literature parameter values, which were used to generate the time series, starting from the set of initial parameter value guesses with search ranges shown in Table 3. AMPGO returned the set of parameter values, rounded to three decimal places, displayed in Table 4, while DE returned the set of parameter values, rounded to three decimal places, displayed in Table 5. Their respective fitted solutions are shown in Figs. (8) and (9).

As evidenced by the values displayed in Tables 4 and 5, as well as the action potential fits seen in Figs. (8) and (9), while both optimization methods were effective in fitting the parameters, DE was superior. AMPGO was able to effectively recover only one value, E_{K}, while DE was able to effectively recover six values, all except for $\bar{g}_{\mathrm{Na}}$. However, the DE approximation of $\bar{g}_{\mathrm{Na}}$ was still more accurate to the ground

Initial Guesses	Search Ranges	Description
$C_m = 0.1\frac{\mu F}{cm^2}$	$0.1\frac{\mu F}{cm^2}$ to $2.0\ \frac{\mu F}{cm^2}$	Membrane capacitance
$\bar{g}_{\mathrm{Na}} = 111\frac{mS}{cm^2}$	$110\frac{mS}{cm^2}$ to $150\frac{mS}{cm^2}$	Sodium maximum conductance
$\bar{g}_{\mathrm{K}} = 30.1\frac{ms}{cm^2}$	$30\frac{ms}{cm^2}$ to $40\frac{ms}{cm^2}$	Potassium maximum conductance
$\bar{g}_L = 0.1\frac{ms}{cm^2}$	$0.1\frac{ms}{cm^2}$ to $0.5\frac{ms}{cm^2}$	Leak maximum conductance
$E_{\mathrm{Na}} = 41.0mV$	$40mV$ to $55mV$	Sodium reversal potential
$E_{\mathrm{K}} = -89.0mV$	$-90mV$ to $-55mV$	Potassium reversal potential
$E_L = -79mV$	$-80mV$ to $-50mV$	Leak reversal potential

Table 3: Parameter value initializations and search ranges of the standard HH model.

Parameters	Description
$C_m = 0.657 \frac{\mu F}{cm^2}$	Membrane capacitance
$\bar{g}_{\text{Na}} = 136.889 \frac{mS}{cm^2}$	Sodium maximum conductance
$\bar{g}_{\text{K}} = 38.744 \frac{ms}{cm^2}$	Potassium maximum conductance
$\bar{g}_L = 0.417 \frac{ms}{cm^2}$	Leak maximum conductance
$E_{\text{Na}} = 40.952 mV$	Sodium reversal potential
$E_{\text{K}} = -77.044 mV$	Potassium reversal potential
$E_L = -60.865 mV$	Leak reversal potential

Table 4: AMPGO's fitted parameter values of the standard HH model to the synthetically generated data.

Parameters	Description
$C_m = 1.011 \frac{\mu F}{cm^2}$	Membrane capacitance
$\bar{g}_{\text{Na}} = 131.937 \frac{mS}{cm^2}$	Sodium maximum conductance
$\bar{g}_{\text{K}} = 36.280 \frac{ms}{cm^2}$	Potassium maximum conductance
$\bar{g}_L = 0.334 \frac{ms}{cm^2}$	Leak maximum conductance
$E_{\text{Na}} = 49.944 mV$	Sodium reversal potential
$E_{\text{K}} = -76.907 mV$	Potassium reversal potential
$E_L = -55.271 mV$	Leak reversal potential

Table 5: DE's fitted parameter values of the standard HH model to the synthetically generated data.

truth value of 120 $\frac{mS}{cm^2}$ than AMPGO's approximation. Additionally, AMPGO needed 61,400 function evaluations and 634.33 seconds to optimize these parameters, while DE only needed 16,001 function evaluations and 89.03 seconds to optimize the same parameters more accurately. Based on these results, it is clear that DE was the superior optimization method for the HH model.

We repeated this process for the SC model, and produced a time series of 120,000 data points spanning 3000 ms using the literature parameter values shown in Table 2 and a current injection of $I_{ext} = 0.03\ nA$ applied from 1000 to 1600 ms. We then treated this time series like empirical stimulus response current-clamp data, where the parameters were unknown. We used both AMPGO and DE methods to recover ten parameter values initialized at the values with the respective search ranges displayed in Table 6.

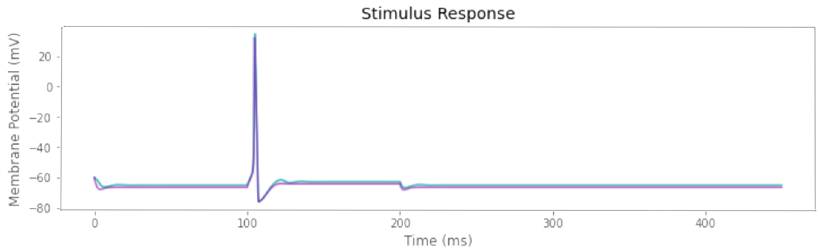

Figure 8: AMPGO was able to successfully approximate all seven parameter values of the HH model in a general manner but could only effectively recover a single parameter from the synthetically generated HH dataset. It produced a very good match of the model solution (magenta) from the synthetic dataset (cyan). The curves appear purple when overlapping.

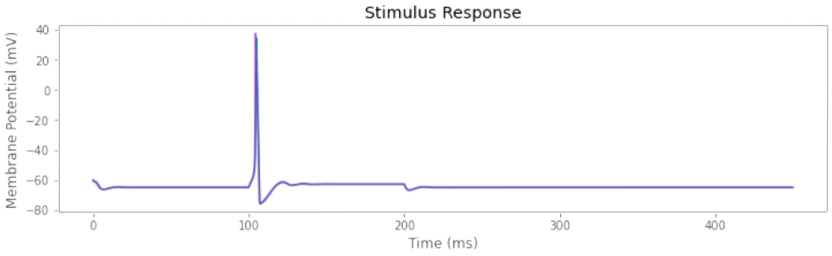

Figure 9: DE was able to successfully approximate all seven parameter values of the HH model in a general manner, effectively recovering six parameters from the synthetically generated HH dataset. It produced a virtually indistinguishable match of the model solution (magenta) from the synthetic dataset (cyan). The curves appear purple when overlapping.

Initial Guesses	Search Ranges	Description
$\bar{g}_{\mathrm{Na}_f} = 1.01\mu S$	$1.00\mu S$ to $5.00\mu S$	Fast Na^+ conductance
$\bar{g}_{\mathrm{Na}_s} =$ 1E-4μS	1E-5μS to 1E-4μS	Slow Na^+ conductance
$\bar{g}_{\mathrm{K}} =$ 9.9E-3μS	1E-4μS to 9.9E-3μS	Delayed rectifier K^+ conductance
$\bar{g}_{B,\mathrm{Na}} =$ 1E-3μS	1E-5μS to 1E-3μS	Background Na^+ conductance
$\bar{g}_A =$ 1E-2μS	1E-3μS to 5E-2μS	Early transient K^+ conductance
$\bar{g}_D =$ 1.9E-2 μS	1E-3μS to 2E-2μS	Inactivating delay K^+ conductance
$\bar{g}_{\mathrm{K,Ca}} =$ 2E-3μS	1E-4μS to 9.9E-3μS	Ca^{2+}-activated K^+ conductance
$\bar{g}_{B,\mathrm{Ca}} =$ 1E-5μS	1E-5μS to 1E-4μS	Background Ca^{2+} conductance
$\bar{g}_{\mathrm{Ca}_t} =$ 1E-4μS	1E-4μS to 1E-3μS	Transient Ca^{2+} conductance
$\bar{g}_{\mathrm{Ca}_n} =$ 1E-3μS	1E-3μS to 1E-2μS	Long-lasting Ca^{2+} conductance

Table 6: Initializations and search ranges of the conductances for the SC model [2].

Parameters	Description
$\bar{g}_{\mathrm{Na}_f} = 1.390\mu S$	Fast Na^+ conductance
$\bar{g}_{\mathrm{Na}_s} = 1.584\text{E-}5\mu S$	Slow Na^+ conductance
$\bar{g}_{\mathrm{K}} = 9.878\text{E-}3\mu S$	Delayed rectifier K^+ conductance
$\bar{g}_{B,\mathrm{Na}} = 5.583\text{E-}4\mu S$	Background Na^+ conductance
$\bar{g}_A = 4.298\text{E-}2\mu S$	Early transient K^+ conductance
$\bar{g}_D = 1.389\text{E-}2\ \mu S$	Inactivating delay K^+ conductance
$\bar{g}_{\mathrm{K,Ca}} = 1.006\text{E-}4\mu S$	Ca^{2+}-activated K^+ conductance
$\bar{g}_{B,\mathrm{Ca}} = 3.224\text{E-}5\mu S$	Background Ca^{2+} conductance
$\bar{g}_{\mathrm{Ca}_t} = 1.115\text{E-}4\mu S$	Transient Ca^{2+} conductance
$\bar{g}_{\mathrm{Ca}_n} = 2.751\text{E-}3\mu S$	Long-lasting Ca^{2+} conductance

Table 7: AMPGO's fitted parameter values of the SC model to synthetically generated data.

Parameters	Description
$\bar{g}_{\mathrm{Na}_f} = 2.112\mu S$	Fast Na^+ conductance
$\bar{g}_{\mathrm{Na}_s} = 7.566\text{E-}5\mu S$	Slow Na^+ conductance
$\bar{g}_{\mathrm{K}} = 5.795\text{E-}3\mu S$	Delayed rectifier K^+ conductance
$\bar{g}_{B,\mathrm{Na}} = 4.248\text{E-}4\mu S$	Background Na^+ conductance
$\bar{g}_A = 4.504\text{E-}2\mu S$	Early transient K^+ conductance
$\bar{g}_D = 8.348\text{E-}3\ \mu S$	Inactivating delay K^+ conductance
$\bar{g}_{\mathrm{K,Ca}} = 8.971\text{E-}3\mu S$	Ca^{2+}-activated K^+ conductance
$\bar{g}_{B,\mathrm{Ca}} = 1.524\text{E-}5\mu S$	Background Ca^{2+} conductance
$\bar{g}_{\mathrm{Ca}_t} = 6.082\text{E-}4\mu S$	Transient Ca^{2+} conductance
$\bar{g}_{\mathrm{Ca}_n} = 1.063\text{E-}3\mu S$	Long-lasting Ca^{2+} conductance

Table 8: DE's fitted parameter values of the SC model to synthetically generated data.

The results of these fittings are shown in Tables 7 and 8, which display the fitted parameters using AMPGO and DE, respectively. Figures (10) and (11) display the fitted solutions of AMPGO and DE, respectively. As can be seen in Fig. (10), AMPGO was unable to produce a good match for the spike portion of the action potential. However, the DE method was able to produce a visually indistinguishable action potential solution with its optimized parameters, as seen in Fig. (11). While in neither case were any parameters recovered nearly identically to their original values, the DE fitting produced parameter values with sufficiently small errors for our purposes, given the visual match. The AMPGO fit took 5,143.99 seconds and

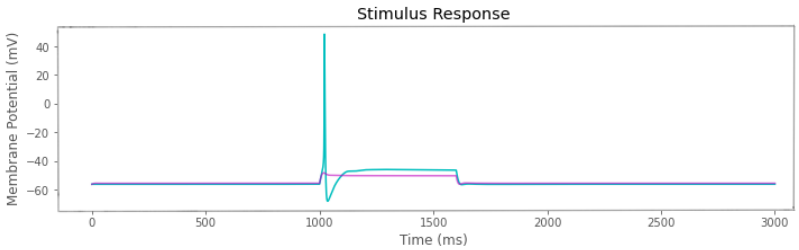

Figure 10: The AMPGO fitting technique was unable to recover the parameter values of the SC model from the synthetically generated SC dataset and failed to reproduce the action potential spike in its model solution (magenta) as seen in the synthetic dataset (cyan). The curves appear purple when overlapping.

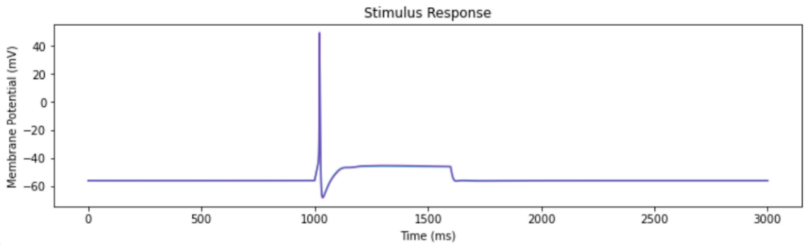

Figure 11: The DE fitting technique was able to successfully approximate all 10 parameter values of the SC model from the synthetically generated SC dataset, producing a visually indistinguishable match of the model solution (magenta) from the synthetic dataset (cyan). The curves appear purple when overlapping.

28,050 function evaluations to complete, while the DE fit took 4,188.97 seconds and 22,001 function evaluations to complete. DE was again able to produce a superior fit for this action potential data in a shorter amount of time and required fewer function evaluations.

Finally, we repeated this process once more for the SC model, this time considering a train of action potentials and extending the fitting process to consider thirteen parameters to provide additional flexibility in the SC model solution. The thirteen parameters considered were the same ten conductances from the SC synthetically generated single-spike data test listed in Table 6 along with $\bar{I}_{\mathrm{NaK}}$, $\bar{I}_{\mathrm{CaP}}$, and $K_{Na,\mathrm{Ca}}$ [2]. We again generated a time series of 120,000 data points spanning 3000 ms using the literature parameter values shown in Table 2 and a current injection of $I_{ext} = 0.04$ nA applied from 1000 to 1600 ms in order to produce the train of action potentials. We again treated this time series like empirical stimulus response current-clamp data, where the parameters were unknown. We used both AMPGO and DE methods to recover these thirteen parameter values initialized at the values with the respective search ranges displayed in Table 9.

The results of these fittings are shown in Tables 10 and 11, which display the fitted parameters using AMPGO and DE, respectively. Figures (12) and (13) display the fitted solutions of AMPGO and DE, respectively. As can be seen in Fig. (12), AMPGO was unable to produce a good match for the spike portion of the action

Initial Guesses	Search Ranges	Description
$\bar{g}_{\mathrm{Na}_f} = 2.00\mu S$	$2.00\mu S$ to $3.00\mu S$	Fast Na^+ conductance
$\bar{g}_{\mathrm{Na}_s} =$ 1E-5μS	1E-5μS to 2E-5μS	Slow Na^+ conductance
$\bar{g}_{\mathrm{K}} =$ 1E-3μS	1E-3μS to 1E-2μS	Delayed rectifier K^+ conductance
$\bar{g}_{B,\mathrm{Na}} =$ 1E-3μS	2E-5μS to 3.5E-4μS	Background Na^+ conductance
$\bar{g}_A =$ 1E-2μS	1E-2μS to 5E-2μS	Early transient K^+ conductance
$\bar{g}_D =$ 1.9E-2 μS	1E-3μS to 2E-2μS	Inactivating delay K^+ conductance
$\bar{g}_{\mathrm{K,Ca}} =$ 5E-3μS	1E-3μS to 9.9E-3μS	Ca^{2+}-activated K^+ conductance
$\bar{g}_{B,\mathrm{Ca}} =$ 1E-4μS	5E-5μS to 1E-4μS	Background Ca^{2+} conductance
$\bar{g}_{\mathrm{Ca}_t} =$ 1E-4μS	1E-4μS to 3E-4μS	Transient Ca^{2+} conductance
$\bar{g}_{\mathrm{Ca}_n} =$ 1E-3μS	1E-3μS to 5E-3μS	Long-lasting Ca^{2+} conductance
$\bar{I}_{\mathrm{NaK}} = 0.21\ nA$	0.20μS to 0.40μS	Na^+-K^+ pump conductance
$\bar{I}_{\mathrm{Ca}P} = 0.02\ nA$	0.02μS to 0.04μS	Ca^{2+} pump conductance
$K_{Na,\mathrm{Ca}} =$ 2E-5 $\frac{nA}{mM^4}$	2E-5μS to 4E-5μS	Na^+-Ca^{2+} exchanger conductance

Table 9: Initializations and search ranges of the conductances for the SC model [2].

potential. However, the DE method was able to produce a visually indistinguishable action potential solution with its optimized parameters, as seen in Fig. (13). While in neither case were any parameters recovered nearly identically to their original values, the DE fitting again produced parameter values with sufficiently small errors for our purposes, given the visual match. The AMPGO fit took 12,569.93 seconds and 51,016 function evaluations to complete, while the DE fit took 6,659.41 seconds and 28,001 function evaluations to complete. DE was again able to produce a superior fit for this action potential data in a shorter amount of time and required fewer function evaluations.

4.2 Fitting the Models to Experimental Nodose Neuron Data

Given the above results and the highly accurate fits from the DE fitting method, we consider our fitting procedure to be robust and validated for optimizing the parameters of the SC model with respect to data. The next step involved replacing the synthetically generated datasets with our experimental rat nodose neuron time series data, shown in Fig. (7). To motivate the relevance of the SC model and its more sophisticated consideration of ion channels and a fluid compartment model, we first attempted to fit our dataset using the HH model. We note that because of the unit difference in current injections described in Sec. 2.3, the current injections from our current-clamp stimulus response dataset needed to be converted to work with the HH model code. The current injection values employed were 0 $\mu A/cm^2$ from approximately 0 to 100 ms, -3.537 $\mu A/cm^2$ from approximately 100 to 350 ms, 0 $\mu A/cm^2$ from approximately 350 to 550 ms, 3.537 $\mu A/cm^2$ from approximately 550 to 800

Parameters	Description
$\bar{g}_{\mathrm{Na}_f} = 2.177\mu S$	Fast Na^+ conductance
$\bar{g}_{\mathrm{Na}_s}$ =1.993E-5μS	Slow Na^+ conductance
$\bar{g}_{\mathrm{K}} = 1.141\text{E-}3\mu S$	Delayed rectifier K^+ conductance
$\bar{g}_{B,\mathrm{Na}} = 1.055\text{E-}4\mu S$	Background Na^+ conductance
$\bar{g}_A = 2.803\text{E-}2\mu S$	Early transient K^+ conductance
$\bar{g}_D = 6.002\text{E-}3\ \mu S$	Inactivating delay K^+ conductance
$\bar{g}_{\mathrm{K,Ca}} = 7.769\text{E-}3\mu S$	Ca^{2+}-activated K^+ conductance
$\bar{g}_{B,\mathrm{Ca}} = 8.5596\text{E-}5\mu S$	Background Ca^{2+} conductance
$\bar{g}_{\mathrm{Ca}_t} = 1.042\text{E-}4\mu S$	Transient Ca^{2+} conductance
$\bar{g}_{\mathrm{Ca}_n} = 3.838\text{E-}3\mu S$	Long-lasting Ca^{2+} conductance
$\bar{I}_{\mathrm{NaK}} = 0.2007\ nA$	Na^+-K^+ pump conductance
$\bar{I}_{\mathrm{Ca}P} = 2.804\text{E-}2\ nA$	Ca^{2+} pump conductance
$K_{Na,\mathrm{Ca}} = 2.209\text{E-}5\ \frac{nA}{mM^4}$	Na^+-Ca^{2+} exchanger conductance

Table 10: AMPGO's fitted parameter values of the SC model to synthetically generated action potential train data.

Parameters	Description
$\bar{g}_{\mathrm{Na}_f} = 2.004\mu S$	Fast Na^+ conductance
$\bar{g}_{\mathrm{Na}_s} = 1.1717\text{E-}5\mu S$	Slow Na^+ conductance
$\bar{g}_{\mathrm{K}} = 2.548\text{E-}3\mu S$	Delayed rectifier K^+ conductance
$\bar{g}_{B,\mathrm{Na}} = 2.901\text{E-}4\mu S$	Background Na^+ conductance
$\bar{g}_A = 2.854\text{E-}2\mu S$	Early transient K^+ conductance
$\bar{g}_D = 1.585\text{E-}2\ \mu S$	Inactivating delay K^+ conductance
$\bar{g}_{\mathrm{K,Ca}} = 6.752\text{E-}3\mu S$	Ca^{2+}-activated K^+ conductance
$\bar{g}_{B,\mathrm{Ca}} = 5.812\text{E-}5\mu S$	Background Ca^{2+} conductance
$\bar{g}_{\mathrm{Ca}_t} = 2.601\text{E-}4\mu S$	Transient Ca^{2+} conductance
$\bar{g}_{\mathrm{Ca}_n} = 1.542\text{E-}3\mu S$	Long-lasting Ca^{2+} conductance
$\bar{I}_{\mathrm{NaK}} = 0.3115\ nA$	Na^+-K^+ pump conductance
$\bar{I}_{\mathrm{Ca}P} = 3.325\text{E-}2\ nA$	Ca^{2+} pump conductance
$K_{Na,\mathrm{Ca}} = 2.043\text{E-}5\ \frac{nA}{mM^4}$	Na^+-Ca^{2+} exchanger conductance

Table 11: DE's fitted parameter values of the SC model to synthetically generated action potential train data.

ms, and 0 $\mu A/cm^2$ from approximately 800 to 819.2 ms. These values correspond to the current injections expressed in the dataset, described in Sec. 3.1.

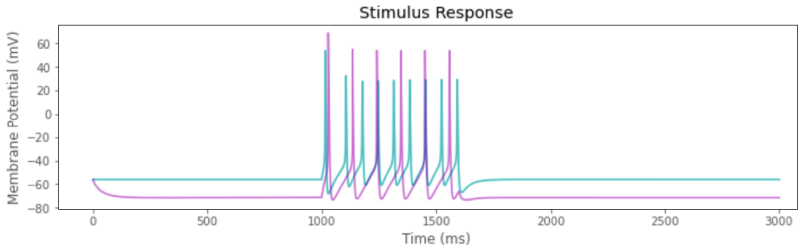

Figure 12: The AMPGO fitting technique was unable to recover the parameter values of the SC model from the synthetically generated SC dataset and failed to produce action potential spikes in its model solution (magenta) that aligned with the spikes observed in the synthetic dataset (cyan). The curves appear purple when overlapping.

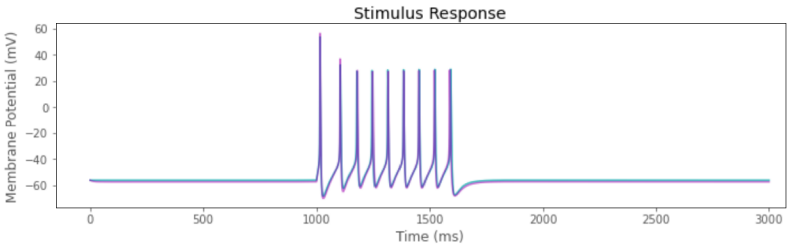

Figure 13: The DE fitting technique was able to successfully approximate all thirteen parameter values of the SC model from the synthetically generated SC dataset, producing a visually indistinguishable match of the model solution (magenta) from the synthetic dataset (cyan). The curves appear purple when overlapping.

Neither AMPGO nor DE were able to reproduce the correct shapes of the action potential data with the HH model, but DE resulted in a slightly superior fit. Table 12 shows the best result of DE fitting with wide parameter search ranges. Figure (14) displays the fitted solution overlaid on the experimental data. This fitting resulted in an unrealistic estimated value of the membrane potential, C_m, of 4.699 $\frac{\mu F}{cm^2}$, rounded to three decimal places. Based on the work done by Schild et al., the membrane capacitance of a nodose neuron should be approximately 1.4 $\mu F/cm^2$ [2].

Figure (15) shows the result of DE fitting with a more realistic parameter search range for C_m. This resulted in a value of the membrane potential, C_m, of approximately 1.488, rounded to three decimal places. With this value, however, the HH model entirely removed the spikes at the end, resulting in an even poorer fit.

Having demonstrated that the HH model was insufficient for characterizing our dataset, we sought to use the SC model to attempt to replicate the time series from our dataset. Figure (16) shows the solution to the SC model with our experimental current injections using the default literature values of all thirteen parameters of interest, as displayed in Table 2. These unfit parameters resulted in a poor reproduction of the stimulus response seen in the dataset.

Our next step, therefore, was to apply the fitting techniques of AMPGO and DE to determine an optimal set of parameter values. Table 13 displays AMPGO's fitted parameter values, and Fig. (17) displays AMPGO's fitted solution using an

Parameters	Description
$C_m = 4.699 \frac{\mu F}{cm^2}$	Membrane capacitance
$\bar{g}_{\text{Na}} = 17.235 \frac{mS}{cm^2}$	Sodium maximum conductance
$\bar{g}_{\text{K}} = 1.061 \frac{ms}{cm^2}$	Potassium maximum conductance
$\bar{g}_L = 0.165 \frac{ms}{cm^2}$	Leak maximum conductance
$E_{\text{Na}} = 78.779mV$	Sodium reversal potential
$E_{\text{K}} = -117.195mV$	Potassium reversal potential
$E_L = -50.803mV$	Leak reversal potential

Table 12: DE's fitted parameter values of the standard HH model to the empirical rat nodose neuron current-clamp data.

error tolerance of 1E-15 overlaid on the dataset. While AMPGO's fit was able to produce three action potential spikes in the fourth current injection time interval of the stimulus response, these spikes were not aligned with the spikes observed in the dataset. The AMPGO fitted parameters also cause a larger drop in voltage during the second current injection interval than was observed in the dataset. Lower tolerance requirements did not yield any improvement in the fits. Table 14 displays DE's fitted parameter values, and Figure (18) displays DE's fitted solution overlaid on the dataset. DE was able to produce a tighter fit for the first three current injection intervals but was only able to generate a single spike in the fourth current injection interval.

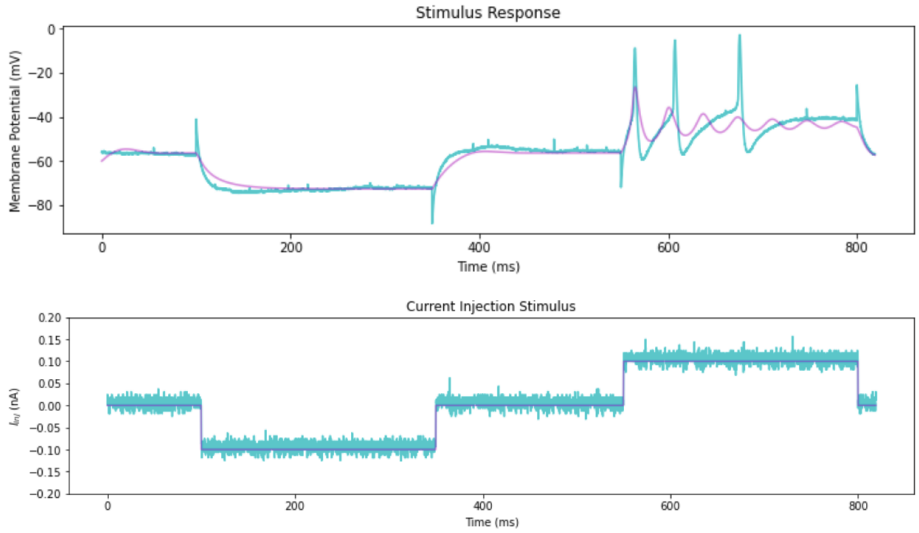

Figure 14: The HH model was not able to reproduce the train of spikes at the end of the stimulus response dataset. This was the best fit done using DE. It yielded an unrealistic value of approximately $C_m = 4.699 \frac{\mu F}{cm^2}$, rounded to three decimal places.

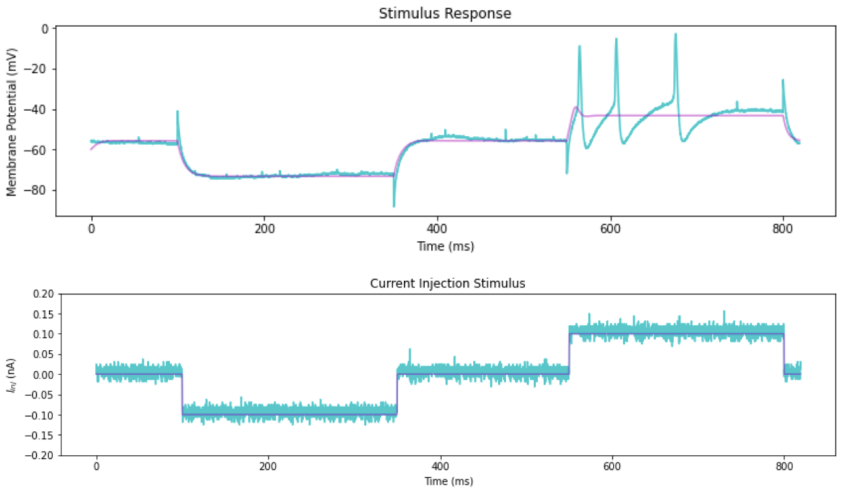

Figure 15: The HH model was not able to reproduce the train of spikes in the fourth current injection interval of the stimulus response dataset when C_m was limited to a realistic search range.

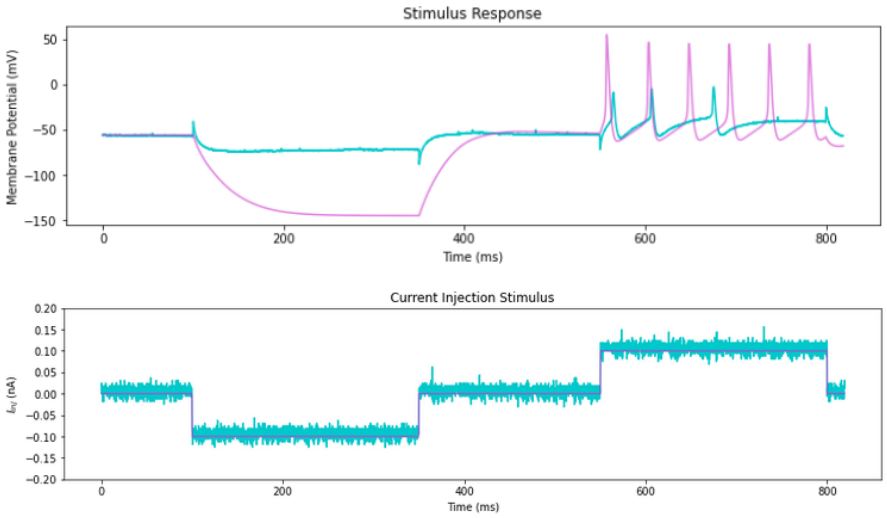

Figure 16: The unfitted default literature values of 13 of the SC model parameters from Table 2 produce a solution (magenta) that does not match the stimulus response data (cyan).

4.2.1 Current Injection Study

As a final analysis on reproducing the stimulus response observed in the dataset, given that DE has thus far provided overall superior parameter fits for our tests, we performed a current injection study with the parameters yielded from the DE fit in

Parameters	Description
$\bar{g}_{\mathrm{Na}_f} = 2.651\ \mu S$	Fast Na^+ conductance
$\bar{g}_{\mathrm{Na}_s} = 1.804\text{E-}5 \mu S$	Slow Na^+ conductance
$\bar{g}_{\mathrm{K}} = 3.309\text{E-}2 \mu S$	Delayed rectifier K^+ conductance
$\bar{g}_{B,\mathrm{Na}} = 7.912\text{E-}4 \mu S$	Background Na^+ conductance
$\bar{g}_A = 4.581\text{E-}3 \mu S$	Early transient K^+ conductance
$\bar{g}_D = 1.341\text{E-}3\ \mu S$	Inactivating delay K^+ conductance
$\bar{g}_{\mathrm{K,Ca}} = 5.053\text{E-}3 \mu S$	Ca^{2+}-activated K^+ conductance
$\bar{g}_{B,\mathrm{Ca}} = 5.848\text{E-}5 \mu S$	Background Ca^{2+} conductance
$\bar{g}_{\mathrm{Ca}_t} = 4.481\text{E-}4 \mu S$	Transient Ca^{2+} conductance
$\bar{g}_{\mathrm{Ca}_n} = 1.390\text{E-}3 \mu S$	Long-lasting Ca^{2+} conductance
$\bar{I}_{\mathrm{NaK}} = 0.3866\ nA$	Na^+-K^+ pump conductance
$\bar{I}_{\mathrm{Ca}P} = 3.522\text{E-}2\ nA$	Ca^{2+} pump conductance
$K_{Na,\mathrm{Ca}} = 4.877\text{E-}5\ \frac{nA}{mM^4}$	Na^+-Ca^{2+} exchanger conductance

Table 13: AMPGO's fitted parameter values of the SC model to empirical rat nodose neuron current-clamp data.

Parameters	Description
$\bar{g}_{\mathrm{Na}_f} = 2.000\ \mu S$	Fast Na^+ conductance
$\bar{g}_{\mathrm{Na}_s} = 1.562\text{E-}5 \mu S$	Slow Na^+ conductance
$\bar{g}_{\mathrm{K}} = 3.587\text{E-}2 \mu S$	Delayed rectifier K^+ conductance
$\bar{g}_{B,\mathrm{Na}} = 9.978\text{E-}4 \mu S$	Background Na^+ conductance
$\bar{g}_A = 4.923\text{E-}3 \mu S$	Early transient K^+ conductance
$\bar{g}_D = 1.933\text{E-}3\ \mu S$	Inactivating delay K^+ conductance
$\bar{g}_{\mathrm{K,Ca}} = 8.6851\text{E-}3 \mu S$	Ca^{2+}-activated K^+ conductance
$\bar{g}_{B,\mathrm{Ca}} = 9.979\text{E-}5 \mu S$	Background Ca^{2+} conductance
$\bar{g}_{\mathrm{Ca}_t} = 4.891\text{E-}4 \mu S$	Transient Ca^{2+} conductance
$\bar{g}_{\mathrm{Ca}_n} = 1.871\text{E-}3 \mu S$	Long-lasting Ca^{2+} conductance
$\bar{I}_{\mathrm{NaK}} = 0.4431\ nA$	Na^+-K^+ pump conductance
$\bar{I}_{\mathrm{Ca}P} = 2.294\text{E-}2\ nA$	Ca^{2+} pump conductance
$K_{Na,\mathrm{Ca}} = 4.179\text{E-}5\ \frac{nA}{mM^4}$	Na^+-Ca^{2+} exchanger conductance

Table 14: DE's fitted parameter values of the SC model to empirical rat nodose neuron current-clamp data.

Fig. (18), found in Table 14. This study involved modifying the current injections within the experimentally recorded noise range, operating under the assumption that

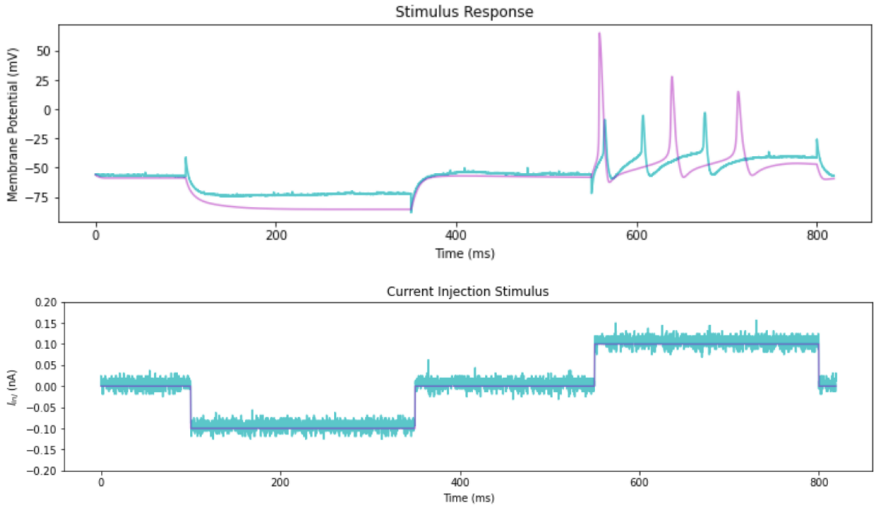

Figure 17: The result (magenta) of a 13-parameter search using AMPGO initialized at the default parameter values from Table 2 with an error tolerance of 1E-15. The parameter optimization method provided a significantly improved solution over the solution using default parameter values in Fig. (16).

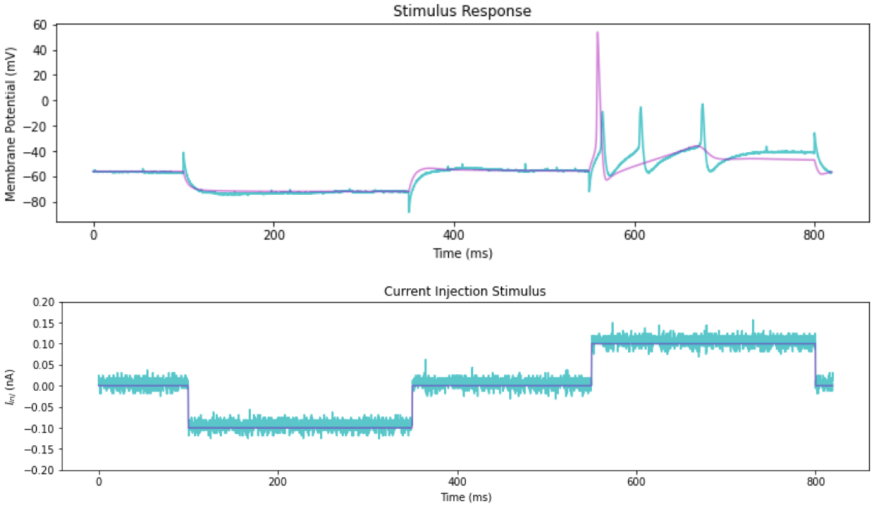

Figure 18: The result (magenta) of a 13-parameter search using DE initialized at the default parameter values from Table 2. The parameter optimization method provided a significantly improved solution over the solution using default parameter values in Fig. (16).

the nodose neuron could have been responding to any current value within that range. We tested several combinations of viable current injections. This was done to see if slightly different current injection values, rather than further altered parameter values, could provide a superior fit from the SC model to the observed stimulus response.

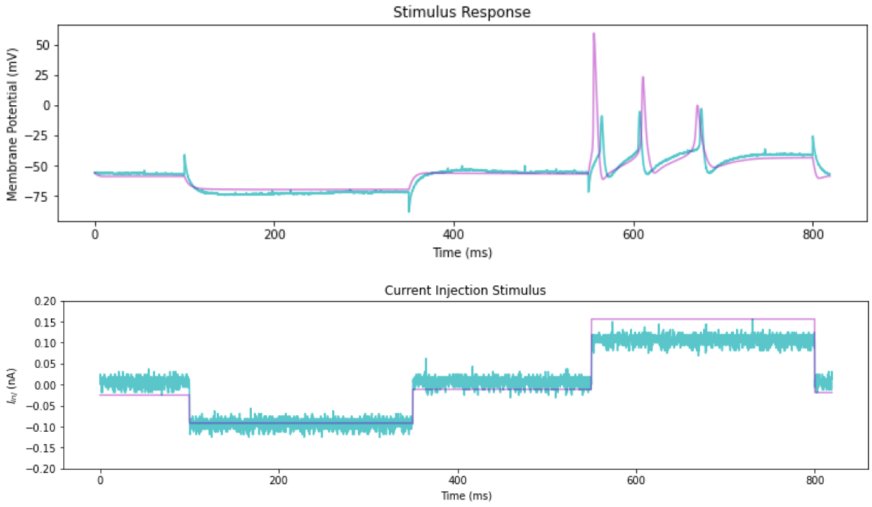

Figure 19: The result of applying a set of modified current injections to the parameters from Fig. (18). This method provided our single best match for the dataset. However, it was still unable to replicate the smaller amplitudes and slightly increasing pattern of the experimental stimulus response spikes.

Using a combination of the minimum current value on the first injection interval, the average current value on the second injection interval, a manually determined current value of -0.11 nA, which was slightly above the minimum value for the third injection interval, the maximum current value on the fourth injection interval, and the minimum current value on the final injection interval, we were able to obtain our best looking fit for the observed dataset, shown in Fig. (19). This demonstrates that the SC model has, in theory, the capacity to yield a solution of a similar form as our experimentally recorded stimulus response values but may require slightly different current injection values.

5 Summary and Remarks

In this work, we developed a methodology for fitting the parameters of excitable cell models to real-world data. This methodology enables us to evaluate a model's capacity to characterize data, as well as gain an understanding of its strengths and weaknesses. Such a tool is useful in testing assumptions that were made within a model and what might be improved for future model improvement.

We used this methodology to evaluate the HH and SC models of neuronal dynamics with respect to rat A-type nodose neuron current-clamp data. First, we established that the parameter optimization techniques we employed here were valid by using these techniques to recover the parameters of the HH model from a synthetic dataset generated by the HH model and to recover the parameters of the SC model from a synthetic dataset generated by the SC model. Then we applied these techniques to optimize the parameters of the HH and SC models with respect to our

nodose neuron dataset. As a result, we were able to show through the AMPGO and DE fitting methods that the SC model could provide a better characterization of the stimulus response behavior observed in a real-world dataset than the HH model. This demonstrated that the SC model serves as a valid extension of the HH model and improves upon the Nobel Prize-winning work's ability to replicate neuronal electrical signatures.

We also showed that despite its superior ability to replicate the behavior of our stimulus response dataset, the SC model with fitted parameters alone could not completely characterize the current-clamp dataset. Using modified current injections that deviated from the intended injection values but were within the range of noise observed in the data, we obtained a superior fit overall. The DE error minimization method worked very well, especially with respect to synthetic data that the model had the capacity to replicate perfectly. Even with the DE method, however, we were unable to obtain a perfect fit with respect to the data. This result may demonstrate a limitation of the SC model in being able to replicate certain neuronal signatures.

Future work in evaluating the SC model may expand into using datasets collected of A-type and C-type rat vagal afferent neurons under different current injection conditions, allowing us an opportunity to establish parameters across multiple datasets. Additional stimulus response datasets may also be collected from rats with varying blood pressure conditions. As the baroreceptor neurons are involved in regulating an organism's blood pressure, their activity may differ in organisms with hypertension, for example. This difference in activity may be encapsulated by significant differences in parameter values of the SC model between a control group of rats without hypertension, like the ones used in this study, and a test group of hypertensive rats.

Future work may also involve improvements to the SC model itself, perhaps considering time- or current-varying parameters rather than constant parameters as we used. This may be able to incorporate more of the underlying cellular dynamics, which were not able to be characterized in this work, and would additionally remove the restriction on the fitting method of having to identify a single combination of parameters that work well for the entire time series or across different current values. These directions may be able to further extend the predictive range of the HH and SC models to more specialized neuron types and continue to help us model and understand neuronal dynamics.

Hodgkin and Huxley produced foundational work in neurophysiology with the invention of their model. The Schild et al. extension of the system builds upon that work by allowing for an advanced study of neuronal dynamics. A methodology for evaluating these models offers us an opportunity to take a step closer to further characterizing the behavior of neurons using parameter optimization techniques. Using the methodology detailed in this project, the parameter estimations of neuronal models may be improved, or their limitations further analyzed in pursuit of the development of higher efficacy models. With these models, we may continue to better understand neuronal dynamics and support the application of this information to medical and scientific innovations.

References

[1] A. L. Hodgkin and B. Katz, "The effect of sodium ions on the electrical activity of the giant axon of the squid," The Journal of Physiology, vol. 108, no. 1, p. 37, 1949.

[2] J. H. Schild, J. W. Clark, M. Hay, D. Mendelowitz, M. C. Andersen, and D. Kunze, "A- and C- type rat nodose sensory neurons: Model interpretations of dynamic discharge characteristics," Journal of Neurophysiology, vol. 71, no. 6, pp. 2338–2357, 1994.

[3] G. Wulfram, M. W. Kistler, R. Naud, and L. Paninski, Neuronal Dynamics. Cambridge University Press, 2014.

[4] A. L. Hodgkin and A. F. Huxley, "Action potentials recorded from inside a nerve fibre," Nature, vol. 144, no. 3651, p. 710–711, 1939.

[5] A. L. Hodgkin and A. F. Huxley, "A quantitative description of membrane current and its application to conduction and excitation in nerve," The Journal of Physiology, vol. 117, no. 4, pp. 500–544, 1952.

[6] H. Zhuo, H. Ichikawa, and C. Helke, "Neurochemistry of the nodose ganglion," Progress in Neurobiology, vol. 52, no. 2, pp. 79–107, 1997.

[7] A. Alić, "Modeling the dynamics of excitable cells," May 2022.

[8] O. Stax, Y. Avissar, J. C., J. DeSaix, V. Jurukovski, and C. Rye, Biology. OpenStax College, Rice University, 2016.

[9] J. Moini, N. Avgeropoulos, and M. Samsam, Epidemiology of Brain and Spinal Tumors. Elsevier Science, 2021.

[10] V. Ramachandran, Encyclopedia of the Human Brain. Elsevier Science, 2002.

[11] A. Citri and R. C. Malenka, "Synaptic plasticity: Multiple forms, functions, and mechanisms," Neuropsychopharmacology, vol. 33, no. 1, p. 18–41, 2007.

[12] H. M. Stauss, "Baroreceptor reflex function," American Journal of Physiology-Regulatory, Integrative and Comparative Physiology, vol. 283, no. 2, 2002.

[13] L. Squire, Encyclopedia of Neuroscience. No. v. 3 in Encyclopedia of Neuroscience, Elsevier/Academic Press, 2009.

[14] V. Snitsarev, C. A. Whiteis, M. W. Chapleau, and F. M. Abboud, "Mechano- and chemosensitivity of rat nodose neurones - selective excitatory effects of prostacyclin," The Journal of Physiology, vol. 582, no. 1, p. 177–194, 2007.

[15] B. G. Kornreich, "The patch clamp technique: Principles and technical considerations," Journal of Veterinary Cardiology, vol. 9, no. 1, pp. 25–37, 2007.

[16] K. Ahnert, M. Mulansky, T. E. Simos, G. Psihoyios, C. Tsitouras, and Z. Anastassi, "Odeint – solving ordinary differential equations in c++," AIP Conference Proceedings, 2011.

[17] L. Lasdon, A. Duarte, F. Glover, M. Laguna, and R. Martí, "Adaptive memory programming for constrained global optimization," Computers Operations Research, vol. 37, no. 8, pp. 1500–1509, 2010. Operations Research and Data Mining in Biological Systems.

[18] K. Fleetwood, "An introduction to differential evolution," in Proceedings of mathematics and statistics of complex systems (MASCOS) one day symposium, 26th November, Brisbane, Australia, pp. 785–791, 2004.

[19] R. Storn and K. Price Journal of Global Optimization, vol. 11, no. 4, p. 341–359, 1997.

6 Appendix

$I_{\text{Ca},t}$: Low Threshold, Transient Calcium Current
$$I_{\text{Ca},t} = \bar{g}_{\text{Ca},t} d_t f_t (V - E_{\text{Ca}})$$
$$\dot{d}_t = \frac{d_{t\infty} - d_t}{\tau_{d_t}} \qquad \dot{f}_t = \frac{f_{t\infty} - f_t}{\tau_{f_t}} \qquad E_{\text{Ca}} = \frac{RT}{Z_{\text{Ca}}} \ln \frac{[\text{Ca}^{2+}]_s}{[\text{Ca}^{2+}]_i} - 78.7$$
$$\tau_{d_t} = 22.0 \exp(-(0.052)^2 (V + 68.0)^2) + 2.5$$
$$\tau_{f_t} = 103.0 \exp(-(0.050)^2 (V + 58.0)^2) + 12.5$$
$$d_{t\infty} = \frac{1.0}{1.0 + \exp\left(\frac{V + 54.0}{-5.75}\right)} \qquad f_{t\infty} = \frac{1.0}{1.0 + \exp\left(\frac{V + 68.0}{6.0}\right)}$$

$I_{\text{Ca},n}$: High Threshold, Long-Lasting Calcium Current
$$I_{\text{Ca},n} = \bar{g}_{\text{Ca},n} d_n (0.55 f_{n1} + f_{n2} (V - E_{\text{Ca}})$$
$$\dot{d}_n = \frac{d_{n\infty} - d_n}{\tau_{d_n}} \qquad \dot{f}_{n1} = \frac{f_{n1\infty} - f_{n1}}{\tau_{f_{n1}}} \qquad \dot{f}_{n2} = \frac{f_{n2\infty} - f_{n2}}{\tau_{f_{n2}}}$$
$$\tau_{d_n} = 3.21 \exp(-(0.042)^2 (V + 31.0)^2) + 0.395$$
$$\tau_{f_{n1}} = 33.5 \exp(-(0.0395)^2 (V + 30.0)^2) + 5.0$$
$$\tau_{f_{n2}} = 225.0 \exp(-(0.0275)^2 (V + 40.0)^2) + 75.0$$
$$d_{n\infty} = \frac{1.0}{1.0 + \exp\left(\frac{V + 20.0}{-4.5}\right)} \qquad r_n = \frac{0.2}{1.0 + \exp\left(\frac{V + 5.0}{-10}\right)}$$
$$f_{n1\infty} = \frac{1.0}{1.0 + \exp\left(\frac{V + 20.0}{25.0}\right)} \qquad f_{n2\infty} = r_n + \frac{1.0}{1.0 + \exp\left(\frac{V + 5.0}{-10.0}\right)}$$

Table 15: Inward Calcium Currents. Two calcium ion currents have been identified in rat nodose sensory neurons: one exhibiting transient dynamics $I_{\text{Ca},t}$; and one exhibiting long-lasting dynamics $I_{\text{Ca},n}$ [2, 7].

I_{Na_f}: Fast, TTX Sensitive Sodium Current
$I_{\mathrm{Na}_f} = \bar{g}_{\mathrm{Na}_f} m_f^3 h_f (V - E_{\mathrm{Na}})$
$\dot{m}_f = \frac{m_{f\infty} - m_f}{\tau_{m_f}} \qquad \dot{h}_f = \frac{h_{f\infty} - h_f}{\tau_{h_f}}$
$\tau_{m_f} = 1.15 \exp(-(0.06)^2 (V + 40.0)^2) + 0.21$
$\tau_{h_f} = 18.0 \exp((0.043)^2 (V + 62.5)^2) + 1.35$
$m_{f\infty} = \frac{1.0}{1.0 + \exp\left(\frac{V + 31.6}{-6.98}\right)} \qquad h_{f\infty} = \frac{1.0}{1.0 + \exp\left(\frac{V + 66.0}{-5.97}\right)}$
I_{Na_s}: Slower, TTX Insensitive Sodium Current
$I_{\mathrm{Na}_s} = \bar{g}_{\mathrm{Na}_s} m_s^3 h_s (V - E_{\mathrm{Na}})$
$\dot{m}_s = \frac{m_{s\infty} - m_s}{\tau_{m_s}} \qquad \dot{h}_s = \frac{h_{s\infty} - h_s}{\tau_{h_s}}$
$\tau_{m_s} = 1.45 \exp(-(0.058)^2 (V + 14.5)^2) + 0.26$
$\tau_{h_s} = 10.75 \exp((0.067)^2 (V + 13.5)^2) + 3.15$
$m_{s\infty} = \frac{1.0}{1.0 + \exp\left(\frac{V + 11.3}{-5.45}\right)} \qquad h_{s\infty} = \frac{1.0}{1.0 + \exp\left(\frac{V + 31.0}{5.2}\right)}$

Table 16: Inward Sodium Currents. Two sodium ion currents have been identified in rat nodose neurons: one large TTX-sensitive current exhibiting fast kinetics I_{Na_f}; and one smaller TTX-insensitive current with slower kinetics I_{Na_s} [2, 7].

I_{K}: Delayed Rectifier
$I_{\mathrm{K}} = \bar{g}_{\mathrm{K}} n (V - E_{\mathrm{K}})$ $\qquad$ $\dot{n} = \frac{n_\infty - n}{\tau_n}$
$\tau_n = \frac{1.0}{(\alpha_n + \beta_n)}$ $\qquad$ $n_\infty = \frac{1.0}{1.0 + \exp\left(\frac{V+14.62}{-18.38}\right)}$
$\alpha_n = \frac{0.001265(V+14.273)}{1.0 - \exp\left(\frac{V+14.273}{-10.0}\right)}$ $\qquad$ $\beta_n = 0.125 \exp\left(\frac{V+55.0}{-2.5}\right)$
I_A: Early Transient Outward Current
$I_A = \bar{g}_A p^3 q (V - E_{\mathrm{K}})$
$\dot{p} = \frac{p_\infty - p}{\tau_p}$ $\qquad$ $\dot{q} = \frac{q_\infty - 1}{\tau_q}$
$\tau_p = 5.0 \exp\left(-(0.22)^2 (V + 65.0)^2\right) + 2.5$
$\tau_q = 100.0 \exp\left(-(0.035)^2 (V + 30.0)^2\right) + 10.5$
$p_\infty = \frac{1.0}{1.0 + \exp\left(\frac{V+28.0}{-28}\right)}$ $\qquad$ $q_\infty = \frac{1.0}{1.0 + \exp\left(\frac{V+58.0}{7.0}\right)}$
I_D: Slowly Inactivating Delay Current
$I_D = \bar{g}_D x^3 y (V - E_{\mathrm{K}})$
$\dot{x} = \frac{x_\infty - x}{\tau_x}$ $\qquad$ $\dot{y} = \frac{y_\infty - y}{\tau_y}$
$\tau_x = 5.0 \exp\left(-(0.022)^2 (V + 65.0)^2\right) + 2.5$ $\qquad$ $\tau_y = 7500.0$
$x_\infty = \frac{1.0}{1.0 + \exp\left(\frac{V+39.59}{-14.68}\right)}$ $\qquad$ $y_\infty = \frac{1.0}{1.0 + \exp\left(\frac{V+48.0}{7.0}\right)}$
$I_{\mathrm{K,Ca}}$: Calcium-Activated Potassium Current
$I_{\mathrm{K,Ca}} = \bar{g}_{\mathrm{K,Ca}} c (V - E_{\mathrm{K}})$ $\qquad$ $\dot{c} = \frac{c_\infty - c}{\tau_c}$
$\alpha_c = 750.0 [\mathrm{Ca}^{2+}]_i \exp\left(\frac{V-10.0}{12.0}\right)$ $\qquad$ $\beta_c = 0.05 \exp\left(\frac{V-10.0}{-60.0}\right)$
$\tau_c = \frac{4.5}{\alpha_c + \beta_c}$ $\qquad$ $c_\infty = \frac{\alpha_c}{\alpha_c + \beta_c}$

Table 17: Outward Potassium Currents. Four potassium ion currents have been identified in rat nodose neurons: a delayed rectifier current I_{K}; two independent potassium ion currents, one exhibiting rapid kinetics I_A, and another which rapidly activates, but inactivates with slow voltage-independent time constant I_D; and one calcium activated potassium current $I_{\mathrm{K,Ca}}$ [2, 7].

I_B: Background Current
$I_B = I_{B,\mathrm{Na}} + I_{B,\mathrm{Ca}} = \bar{g}_{B,\mathrm{Na}}(V - E_{\mathrm{Na}}) + \bar{g}_{B,\mathrm{Ca}}(V - E_{\mathrm{Ca}})$
$I_{\mathrm{Na,Ca}}$: Sodium-Calcium Exchanger Current
$I_{\mathrm{NaCa}} = I_{\mathrm{NaCa}} \frac{DF_{in} - DF_{out}}{S}$
$S = 1.0 + D_{\mathrm{NaCa}}([\mathrm{Ca}^{2+}]_i [\mathrm{Na}^{+}]_o^r + [\mathrm{Ca}^{2+}]_s [\mathrm{Na}^{+}]_i^r)$
$DF_{in} = [\mathrm{Na}^{+}]_i^r [\mathrm{Ca}^{2+}]_s \exp\left(\frac{(r-2)\gamma VF}{RT}\right)$
$DF_{out} = [\mathrm{Na}^{+}]_o^r [\mathrm{Ca}^{2+}]_i \exp\left(\frac{(r-2)(\gamma-1)VF}{RT}\right)$
$I_{\mathrm{Ca}P}$: Calcium Pump Current
$I_{\mathrm{Ca}P} = \bar{I}_{\mathrm{Ca}P}\left(\frac{[\mathrm{Ca}^{2+}]_i}{[\mathrm{Ca}^{2+}]_i + \mathrm{K}_{M,\mathrm{Ca}P}}\right)$
I_{NaK}: Sodium-Potassium Pump Current
$I_{\mathrm{NaK}} = \bar{I}_{\mathrm{NaK}}\left(\frac{[\mathrm{Na}^{+}]_i}{[\mathrm{Na}^{+}]_i + \mathrm{K}_{M,\mathrm{Na}}}\right)^3 \left(\frac{[\mathrm{K}^{+}]_o}{[\mathrm{K}^{+}]_o + \mathrm{K}_{M,\mathrm{K}}}\right)^2 \left(\frac{V+150}{V+200}\right)$

Table 18: Background, voltage, and concentration-dependent currents. Most excitable cells employ ion exchange mechanisms and ATP dependent pumps to maintain intracellular homeostasis. Active transport of sodium, potassium, and calcium ions is credited to the three mechanisms shown in this table: sodium-calcium exchanger current I_{NaCa}; calcium pump current $I_{\mathrm{Ca}P}$; and sodium-potassium pump current I_{NaK}. The model also includes a background current I_B [2, 7].